






Cite this: *Chem. Soc. Rev.*, 2023, 52, 1288

Antimonene: a tuneable post-graphene material for advanced applications in optoelectronics, catalysis, energy and biomedicine

Jose A. Carrasco,  † Pau Congost-Escoin,  † Mhamed Assebbaan and Gonzalo Abellán  *

The post-graphene era is undoubtedly marked by two-dimensional (2D) materials such as quasi-van der Waals antimonene. This emerging material has a fascinating structure, exhibits a pronounced chemical reactivity (in contrast to graphene), possesses outstanding electronic properties and has been postulated for a plethora of applications. However, chemistry and physics of antimonene remain in their infancy, but fortunately recent discoveries have shed light on its unmatched allotropy and rich chemical reactivity offering a myriad of unprecedented possibilities in terms of fundamental studies and applications. Indeed, antimonene can be considered as one of the most appealing post-graphene 2D materials reported to date, since its structure, properties and applications can be chemically engineered from the ground up (both using top-down and bottom-up approaches), offering an unprecedented level of control in the realm of 2D materials. In this review, we provide an in-depth analysis of the recent advances in the synthesis, characterization and applications of antimonene. First, we start with a general introduction to antimonene, and then we focus on its general chemistry, physical properties, characterization and synthetic strategies. We then perform a comprehensive study on the allotropy, the phase transition mechanisms, the oxidation behaviour and chemical functionalization. From a technological point of view, we further discuss the applications recently reported for antimonene in the fields of optoelectronics, catalysis, energy storage, cancer therapy and sensing. Finally, important aspects such as new scalable methodologies or the promising perspectives in biomedicine are discussed, pinpointing antimonene as a cutting-edge material of broad interest for researchers working in chemistry, physics, materials science and biomedicine.

Received 7th July 2022

DOI: 10.1039/d2cs00570k

rs.c.li/chem-soc-rev

1. Introduction

Since the isolation of phosphorene, the two-dimensional (2D)-pnictogen (P, As, Sb and Bi) science has emerged as one of the main topics in 2D materials.^{1–11} Indeed, 2D materials from group 15 of the periodic table offer a great variety of structures, properties and reactivities as a consequence of the progressive increase in the intensity of the interlayer bonds as one goes down the group, passing from purely van der Waals (vdW) materials such as phosphorene to materials with a marked covalent character that makes them quasi-vdW, as is the case with heavy pnictogens (Sb & Bi).^{12–15} The importance of these interactions in the physical and chemical properties of 2D-pnictogens is crucial and differentiates them from the rest of Xenes. This makes heavy 2D-pnictogens, and antimonene in particular, one of the most attractive materials in the field, as it opens the door to chemically engineer their properties from scratch.

This review provides a comprehensive analysis and updated study of antimonene, a material that since its prediction in 2015 and later isolation in 2016 has attracted increasing attention due to its unique electronic properties (thermoelectric, semiconducting, topological insulator, nonlinear optic, *etc.*) and its unmatched atomic structure and chemical flexibility, which allow its exotic (inter-allotropic) phase engineering. Moreover, this review thoroughly analyses (>200 articles) the state-of-the-art of antimonene research, highlighting the recent progress in its experimental preparation with a strong emphasis on its properties, chemical reactivity, functionalization, and the potential applications reported to date. Despite the fact that there are a few reviews focused on pnictogens as a family of emerging materials, this work intends to address the antimonene state-of-the-art from in-depth and critical chemical points of view. To the best of our knowledge this approach has not been addressed to date. Indeed, in a post-graphene era, antimonene holds great promise for the development of fundamental science such as novel van der Waals (and beyond) heterostructures, molecular interface engineering, DNA sensors, high-performance (opto)electronic devices, modern

Instituto de Ciencia Molecular (ICMol), Universidad de Valencia, Catedrático José Beltrán Martínez, 2, 46980 Paterna, Spain. E-mail: gonzalo.abellan@uv.es

† These authors contributed equally to this article.



Na-ion batteries and many other scientific challenges to come. Scheme 1 summarizes the different synthetic approaches and main applications of this fascinating material, which will be detailed below, including a brief historical note about the origin of antimony and its properties.

1.1 History of antimony and general properties

Antimony (symbol Sb, from the Latin *stibium* and derived from the Greek word referring to the use of stibnite) has been known since ancient times (*ca.* 4000 BC) and has been used in the form

of cosmetics, medications, colouring agent for glass and casting pottery, to name a few. In this sense, ancient Egyptians used antimony in the form of stibnite (Sb_2S_3) as a rouge for lips. Similarly, ancient Romans used stibnite in a medical way or as black eye make-up.¹⁶ The name antimony comes from two different Greek words: *anti*, which means *not* and *monos*, whose meaning refers to *alone*. This compound noun is due to the rare appearance of isolated antimony in nature while is commonly found as combined with both metals and non-metals.



Jose A. Carrasco

Jose Alberto Carrasco obtained his degree in Chemistry from the University of Valencia (UV) in 2012. Afterwards, he received his Master's degree in Nanoscience and Nanotechnology in 2014. From 2014 to 2018 he pursued his PhD supervised by Prof. Eugenio Coronado and Dr. Gonzalo Abellán at the Institute of Molecular Science (ICMol, UV), focusing on inorganic two-dimensional materials. Thereafter, he worked as a postdoctoral fellow in the 2D-Chem group at

ICMol (2019–2020) working on 2D-pnictogens, and at the Institute of Chemical Technology (ITQ) under the supervision of Dr. Antonio Leyva-Pérez, working in catalysis (CSIC-UPV, 2021). Now he is working in his true passion as a teacher of physics and chemistry, sharing his love for science to the younger generations.



Pau Congost-Escoin

Pau Congost-Escoin received his BSc in Biochemistry and Biomedical sciences from the University of Valencia (UV) in 2020, and a Master's degree in Nanoscience and Nanotechnology in 2021, when he started working on 2D materials. He is currently a PhD student in Nanoscience and Nanotechnology at ICMol (UV), under the supervision of Dr. Gonzalo Abellán, working on the biomedical applications of 2D pnictogens. His research interest lies in the

interactions of 2D materials in biological environments and the mechanisms governing them.



Mhamed Assebban

Mhamed Assebban obtained his BSc in Chemical engineering and materials science at the University of Abdelmalek Essaadi in 2009 and his Master's degree in 2011. He obtained his PhD in 2016 at the same university, in a collaborative research project with the University of Bielefeld in Germany, where he developed efficient heterogeneous catalysts for the removal of toxic atmospheric gases. He joined the Zentralinstitut für neue Materialien und Prozesstechnik

(ZMP, FAU) in Germany as a postdoctoral researcher in 2018, and then he moved to the Institute of Molecular Science (ICMol) at the University of Valencia in Spain under the supervision of Dr. Gonzalo Abellán. In 2020 he returned back to occupy the same position at the ZMP in Fürth where he focuses his research work on the study of novel 2D materials by tuning their physical and chemical properties to make them even more suitable for different applications, such as energy storage, catalysis and optoelectronics.

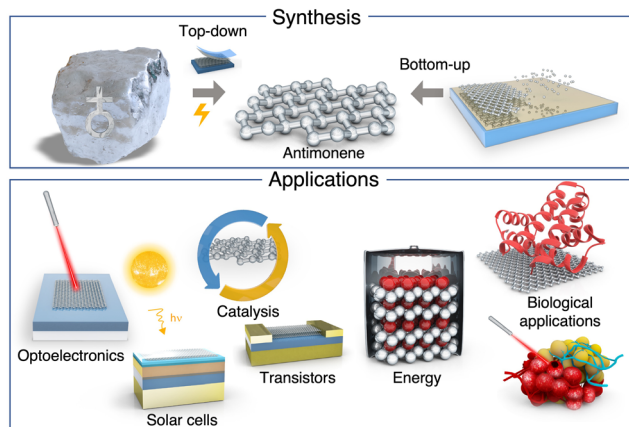


Gonzalo Abellán

Gonzalo Abellán obtained his PhD in nanoscience and nanotechnology in 2014 from the University of Valencia. Afterwards he gained a self-driven Marie Curie Fellowship and joined Prof. Andreas Hirsch's group at the Friedrich-Alexander-Universität, Erlangen-Nürnberg. In 2018 he returned to Spain as an Excellence Distinguished Researcher after getting a GenT-CIDEGENT contract (Generalitat Valenciana), the Ramón y Cajal fellowship, and the ERC Starting

Grant, among others. Gonzalo Abellán's main research activities have been focused on three lines: 2D-pnictogens (group of P, As, Sb and Bi), layered hydroxides, and carbon nanoforms and related hybrid materials, with a special emphasis on energy-related applications. He is the leader of the 2D-Chem research group at the Institute of Molecular Science (ICMol, UV).





Scheme 1 Summary of antimonene synthesis and applications. The image above represents (top) the synthesis of antimonene from bulk antimony or *via* the assembly of antimony atoms on a substrate and (bottom) the applications of antimonene as a multifunctional material. From left to right: optoelectronic devices, solar cells, catalysis, field-effect transistors, energy storage, biomedical applications by binding molecules of interest and destroying carcinogenic cells.

The use of Sb was also described by medieval alchemists in the 15th century. The element intrigued the alchemists due to its similar properties to those of gold and the fact that it cannot be dissolved with aqua regia, hence being a good candidate for its transmutation into gold.¹⁷ During the 16th century, Paracelsus and his followers promoted the use of antimony and other metals as drugs. This statement was in stark contrast with the teachings of Galen (*ca.* 2nd century) who considered the use of metals as poisonous.¹⁸ In this context, the period between *ca.* 1560 and 1660 was coined as the antimony war due to the strong conflict between the Galenic medicine against the medical practices of Paracelsus.

Even though the original discoverer of Sb remains unknown, Nicolas Lémery, a French chemist, was the first one to scientifically study both antimony and its compounds, publishing his findings in 1707. Antimony compounds have been used for centuries in the treatment of schistosomiasis and leishmaniasis;¹⁹ however, one of the most recognisable aspects of antimony is its toxicity,²⁰ since it can even cause death by intoxication and its symptoms are disguised as general gastric disorders. The poisonous activity comes from its ability to be attached to particular enzymes because of its high affinity to the sulphur atoms of the enzyme's active site. Regarding the different species, one of the deadliest compounds of antimony is the gas stibine (SbH_3). Most antimony compounds such as stibine or oxides (Sb_2O_3 , Sb_2O_5 , *etc.*) can be absorbed from the respiratory tract due to the low particle size, therefore being retained in the organism for longer periods than larger particles.²¹

From the economic point of view and regarding the applications of antimony and its compounds, the element is a metalloid with an important impact. The actual annual production is at around 185 000 tonnes per year, with 85% coming from China. Additional producers can be found in countries like

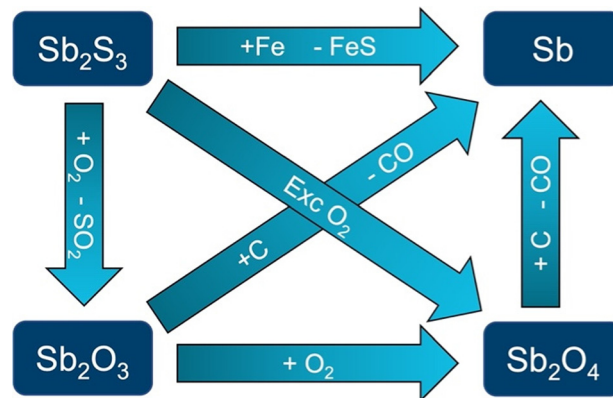


Fig. 1 Schematic representation of the production of elemental antimony from stibnite. Adapted from ref. 23 with permission from John Wiley & Sons, copyright 2011.

Russia, South Africa or Bolivia, among others. The main ores are in the form of stibnite and tetrahydrite, this one being a copper antimony sulfosalt mineral with formula: $(\text{Cu,Fe})_{12}\text{Sb}_4\text{S}_{13}$, which yields Sb as a by-product.¹⁷ Stibnite is easily separated from other minerals due to its low melting point of 546 °C. Afterwards, the roasting of stibnite produces Sb_2O_3 or Sb_2O_4 which can be both reduced to elemental Sb with coke. An alternative method to obtain Sb is to directly reduce the stibnite with scrap iron, followed by a purification procedure with sodium nitrate and sodium carbonate.^{22,23} Fig. 1 schematizes the production of elemental Sb from stibnite.

With respect to the main applications, antimony compounds can be used in different fields such as flame retardants (Sb_2O_3), catalysis (SbF_5), pyrotechnical articles ($\text{Sb}_2\text{S}_3 + \text{H}_2\text{S}$) or in electronics (alloyed with Ga and As).^{17,24} Related to electronic applications, Sb is mainly used in semiconductor devices such as diodes and infrared detectors. Alloying with Pb or other metals can enhance its hardness and strength. In this sense, a wide variety of alloys are described with Na, K, Ag, Au, Mg, Zn or Al, to name a few,²⁵ leading to additional applications like cable and bullet sheathing as well as its use in batteries in the form of a Sb–Pb alloy.²⁶


From the chemical point of view, Sb is considered a metalloid element, a member of the group 15 in the periodic table, *i.e.*, the family of pnictogens and with an electronic configuration of $[\text{Kr}] 4d^{10} 5s^2 5p^3$. Regarding the position of pnictogens in the periodic table, it is not unusual to come across some papers that refer to group VA instead of group 15. Here, we want to point out the fact that this old nomenclature based on roman numbers and capital letters A/B has been discarded by the IUPAC since 1990.²⁷ Therefore, the only correct labelling nowadays for the pnictogen group is 15. Sb can appear in two different forms: while the metallic one is bright, slivery, hard and brittle (and resembles Pb), the non-metallic one is a grey powder. Furthermore, it poorly conducts both electricity and temperature, whereas it shows good stability in dry air and is not affected by dilute acids or alkalis. Additionally, upon cooling, Sb and some of its alloys expand.²⁸ The most common

isotopes, there are 37 known Sb isotopes, with masses that vary from 103 to 139 u. In this context, there are two naturally stable isotopes: Sb-121 (57%) and Sb-123 (43%). Some isotopes are radioactive and produced after fission experiments. Among these, Sb-125 is the longest-lived radioisotope, with a half-life of 2.76 years.³³ Additional elemental parameters of Sb can be found in Table 1.

Concerning the existence of allotropes, elemental bulk Sb has three known allotropes: explosive, black and gray.²² The most common form is the gray allotrope, with a rhombohedral structure like gray arsenic and a typical semi metallic behaviour. Black antimony is analogous to red phosphorus and explosive antimony usually evolve to the gray one after mechanical stress or on heating.³⁴ While other pnictogens such as P and As depict α and β layered stable phases, the heavy pnictogens Sb and Bi have their most stable phase as the β allotrope even though other allotropes are theoretically predicted and recently obtained under certain conditions, which will be detailed below.^{35,36} Fig. 2 summarizes the different layered crystal structures and stable phases.³⁴

After the rise of graphene in 2004,^{37–39} a myriad of new graphene-like two-dimensional (2D) materials have arisen.^{40–43} The number of documents by year related to the topic of 2D materials keeps growing and has reached a maximum of *ca.* 17 000 papers by mid-2022 (source: Scopus). Fig. 3 depicts the total number of papers related specifically to 2D-pnicotegns. This trend is motivated for the outstanding properties of these materials towards new applications in the fields of

Table 1 Elemental parameters for antimony. Some data are extracted from ref. 51

Parameter	Value	Parameter	Value
Year of discovery	Known from <i>ca.</i> 4000 B.C., studied by Nicolas L��mery (1707)	Magnetic type	Diamagnetic
Alchemy symbol		Molar magnetic susceptibility (m ³ mol ^{−1})	−1.327 × 10 ^{−9}
Atomic number	51	Electronic shell	[Kr] 4d ¹⁰ 5s ² 5p ³
Atomic mass (g mol ^{−1})	121.75	Standard potential (V)	0.21 (Sb ³⁺ /Sb) 0.60 (Sb ₂ O ₃ /SbO ⁺) −0.51 (Sb/SbH ₃)
Density (g cm ^{−3})	6.684	Natural isotopes, abundance and radioactive stability	¹²¹ Sb (57.4%, stable) ¹²³ Sb (42.6%, stable)
Melting point (�C)	631	Abundance in Earth’s crust	0.00002%
Boiling point (�C)	1587	Nuclear spin, I	¹²¹ Sb (+5/2) ¹²³ Sb (+7/2)
Heat of fusion (kJ mol ^{−1})	19.7	Ionization energies (kJ mol ^{−1})	
Heat of vaporization (kJ mol ^{−1})	67	M → M ⁺	833.7
Specific heat (J kg ^{−1} K ^{−1})	207	M ⁺ → M ²⁺	1794
Thermal conductivity (W m ^{−1} K ^{−1})	24	M ²⁺ → M ³⁺	2443
Bulk modulus (GPa)	42 GPa	M ³⁺ → M ⁴⁺	4260
Shear modulus (GPa)	20	M ⁴⁺ → M ⁵⁺	5400
Young modulus (GPa)	55	Electron affinity (kJ mol ^{−1})	101
Mohs hardness	3	M → M [−]	
Space group name	R��3m	Electronegativity, � _P (Pauling scale)	2.05
Electrical type	Conductor	Atomic radius (�)	1.82
Electrical conductivity (S m ^{−1})	2.5 × 10 ⁶	Single-bond covalent radius (�)	1.41
Resistivity (m �)	4 × 10 ^{−7}	van der Waals radius (�)	2.20
		Ionic radii (�)	M ³⁺ 0.62 M ⁵⁺ 0.76



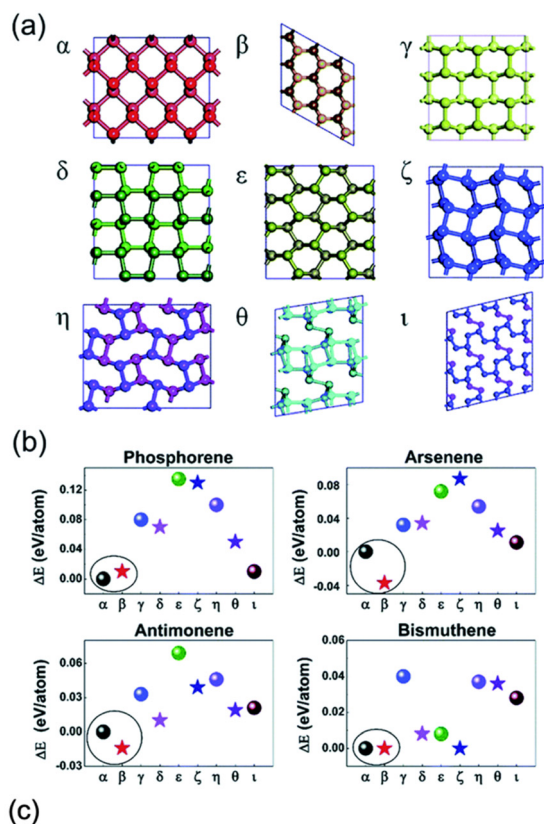


Fig. 2 (a) Typical honeycomb and non-honeycomb structures of 2D pnictogen allotropes. (b) Average binding energies of the different allotropes, highlighting the β phase as the most stable in average. (c) Table summarizing the stable phases of the different pnictogens. While α phase presents a parallel puckered layer with space group of $Cmca$, β phase exhibits parallel buckled layers with the $R\bar{3}m$ space group in a rhombohedral structure. Adapted from ref. 34 with permission from Royal Society of Chemistry, copyright 2018.

energy, electronics, catalysis, topological insulators, thermal management or anisotropic magnetization.⁴⁰

The wide variety of 2D materials that are described in the literature can be divided into three main groups: the layered van der Waals (vdW) solids, the 3D covalent/ionic solids, and the layered ionic solids. This classification is based on the main forces that ensemble the layered structure, *i.e.*, intermolecular van der Waals interactions or electrostatic forces. While in the first group one can find materials such as graphene, boron nitride or layered metal dichalcogenides,^{40,44} the second group is composed of covalent materials that can be exfoliated down

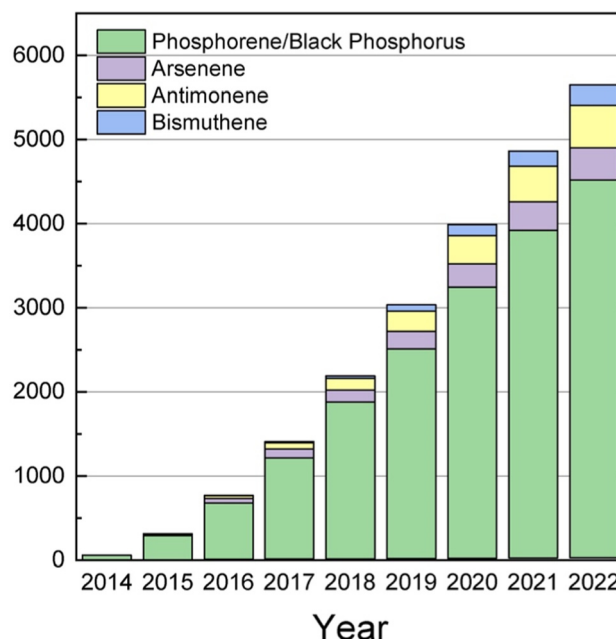


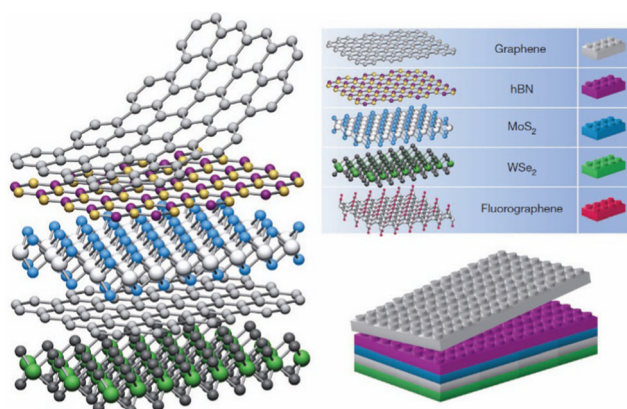
Fig. 3 Graphic showing the cumulative number of papers focused on 2D pnictogens. Data acquired from Scopus on October 2022.

to the 2D limit (*i.e.* germanene) or 3D ionic solids (like iron oxide) that can be exfoliated by controlling parameters such as the energy of cleavage planes or the stabilization energy of the nanolayers. Finally, the third group includes charged 2D layers that are held together, thanks to the presence of cations or anions in the interlayer space. This is the case of layered metal oxides, layered double hydroxides or cation-exchanged layers from Ruddlesden–Popper perovskite-type structures.^{45–50} Table 2 shows some of the reported 2D materials and Fig. 4 depicts how these can be assembled together to build van der Waals heterostructures.

The group of pnictogens (P, As, Sb and Bi) exhibits several allotropes with layered structures, both with rhombohedral and orthorhombic structures.³⁴ In this sense, true van der Waals forces held the layered assembly in the orthorhombic structure, while the interlayer interactions of the rhombohedral counterparts increase concomitantly with the atomic number, *i.e.*, the nature of the pnictogen.⁵³ The first one to be described was phosphorene in 2014, the 2D counterpart of layered black phosphorus, which exhibited great potential as a p-type semiconducting material (Fig. 5). The authors described a few-layer phosphorene field-effect transistor with a channel length of 1.0 μm at room temperature, which displayed a high on-current of 194 mA mm^{-1} together with a high hole field-effect mobility of 286 $\text{cm}^2 \text{V}^{-1} \text{s}^{-1}$ and an on/off ratio of up to 10^4 .⁵⁴ Phosphorene exhibits an orthorhombic crystalline form in which the P atoms are assembled composing hexagonal puckered layers that are sustained thanks to true van der Waals forces. It displays high reactivity as well as a rapid oxidation under ambient conditions leading to the formation of P_xO_y compounds which, in the presence of moisture, leads to the formation of phosphoric acid and related compounds.⁵⁵ Furthermore, it has a modulable

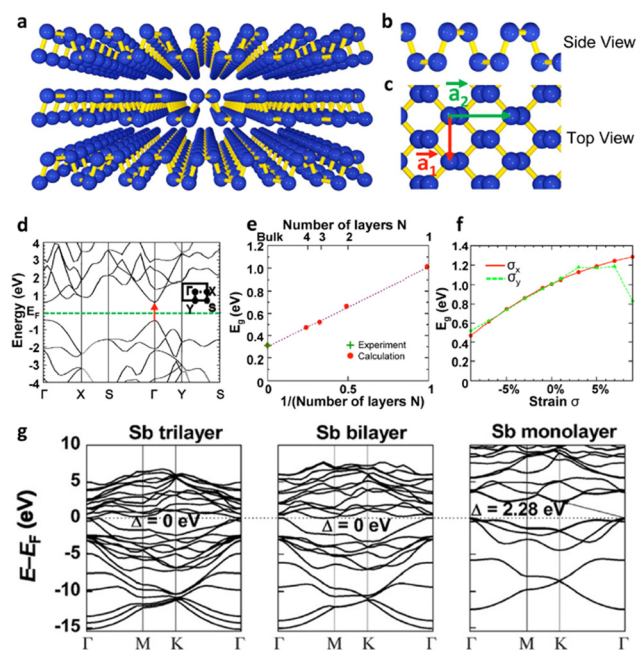
Table 2 Reported monolayers in the literature classified into different families according to its composition. Adapted from ref. 42 and 52

Carbon materials	Graphene	Hexagonal boron nitride (white graphene) and boron carbon nitride	Graphene oxide	Fluorographene
Xenes	Group 13: borophene, gallene	Group 14: graphene, silicene, germanene, stanene	Group 15: phosphorene, arsenene, antimonene, bismuthene	Group 16: selenene, tellurene
2D Chalcogenides	MoS ₂ , WS ₂	Semiconducting dichalcogenides: MoTe ₂ , WTe ₂ , ZrS ₂ , ZrSe ₂ , etc.	Metallic dichalcogenides: NbSe ₂ , NbS ₂ , TaS ₂ , TiS ₂ , NiSe ₂ , etc.	Layered semiconductors: GaSe, GaTe, InSe, Bi ₂ Se ₃ , etc.
2D oxides and hydroxides	MoS ₂ , WSe ₂ Micas Cu oxides, etc.	MoO ₃ , WO ₃ , TiO ₂ , MnO ₂ , V ₂ O ₅ , TaO ₃ , RuO ₂ , etc.	Perovskite-type: LaNb ₂ O ₇ , (Ca,Sr) ₂ Nb ₃ O ₁₀ , Bi ₄ Ti ₃ O ₁₂ , Ca ₂ Ta ₂ TiO ₁₀ , etc.	Simple and double hydroxides: Ni(OH) ₂ , Eu(OH) ₂ , NiFe-LDH, CoAl-LDH, etc.

**Fig. 4** Building van der Waals heterostructures by combining different layers of 2D materials. Adapted from ref. 42.

bandgap that ranges from 0.3 eV to 2.2 eV for bulk and monolayer black phosphorus, respectively.⁵⁶ Since then, phosphorene has been extensively studied, including its exfoliation,^{57–59} its covalent and noncovalent functionalization^{55,60,61} as well as its different applications.^{55,62–65} Analogous 2D pnictogens (arsenene, antimonene and bismuthene) have been also predicted and most of them have been experimentally obtained.^{53,66}

In this sense, it is important to point out that the -ene suffix in these materials (phosphorene, antimonene, bismuthene as well as others such as germanene or silicene) does not refer to a double bond between the individual atoms as in graphene. Nevertheless, these sorts of 2D materials composed of one single element are commonly referred to as Xenes by the scientific community.⁶⁷ The layered structure of As corresponds to rhombohedral gray arsenic, and exhibits a tunable bandgap depending on the number of stacked layers of the material, ranging from a predicted 0.47 to 2.49 eV for a bilayer and a monolayer arrangement, respectively.⁶⁸ Studies concerning arsenene are very scarce; nevertheless, there are some reports regarding the preparation of multilayer arsenene with a rhombohedral structure. For example, in the form of applying nitrogen plasma with indium arsenide, giving rise to the synthesis of multilayer arsenene nanoribbons on the surface of the InAs.⁶⁹ Regarding heavy pnictogens (Sb & Bi), the fact of descending through the group implies an increase in interlayer interactions, going from being purely vdW materials to having a

**Fig. 5** Crystal structure and band structure of few-layer phosphorene. (a) Perspective side view of few-layer phosphorene. (b) and (c) Side and top views of few-layer phosphorene. (d) Theoretical band structure of a phosphorene monolayer calculated using DFT-HSE06. (e) and (f) DFT-HSE06 results for the dependence of the energy gap in few-layer phosphorene on (e) the number of layers and (f) the strain along the x- and y-directions in a monolayer system. (g) Representation of the electronic band structures of antimony trilayers, bilayers, and monolayers calculated using DFT-HSE06. Adapted from ref. 54 with permission from American Chemical Society, copyright 2014 and ref. 76 with permission from John Wiley & Sons, copyright 2015.

marked covalent character. Specifically, group 15 elements (without considering nitrogen) tend to favor the sp^3 hybridization, but in their $ns^2 np^3$ valence configuration they tend to form layered structures showing in-plane covalent bonds together with weaker interlayer bonds, which are purely vdW in the case of phosphorene, but progressively incorporate interlayer orbital hybridization in heavier elements, thus forming quasi-vdW materials. This latter aspect is critical in the case of bismuth, thus precluding its micromechanical exfoliation. Moreover, the strong spin-orbit coupling characteristic of heavy pnictogens results in the fact that both known structures of bismuth (α and β forms) have been reported as topological



This journal is © The Royal Society of Chemistry 2023

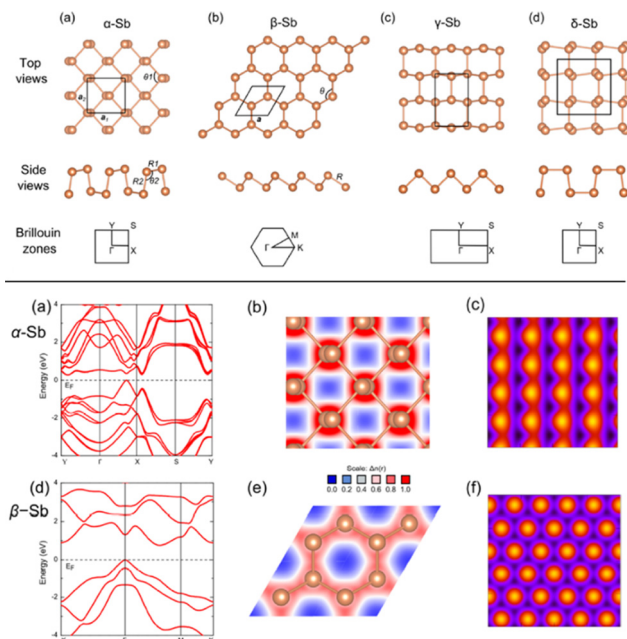


Fig. 6 Top: Structural configurations of antimonene allotropes: (a) α -Sb, (b) β -Sb, (c) γ -Sb, and (d) δ -Sb. Bottom: Electronic properties of (a)–(c) α -Sb and (d)–(f) β -Sb monolayers: (a), (d) band structure, (b), (e) charge density projected in the plane, and (c), (f) simulated scanning tunneling microscopy (STM) images. Adapted from ref. 35 with permission from American Chemical Society, copyright 2015.

with a height of *ca.* 0.9 nm that surely included additional water molecules. It is widely assumed that this layer of adsorbed

water molecules is always present under ambient conditions, with an average thickness of *ca.* 0.6 nm which is present between the deposited flakes of the material and the SiO₂ substrate.^{85,86} These pioneering studies paved the way for the development of the chemistry and physics of antimonene. Henceforth, hundreds of papers dealing with different aspects of antimonene have been published, corroborating the interest generated by this novel 2D material (Fig. 3).

2.2 Properties

Antimonene has been proposed as a good candidate for novel applications due to its outstanding properties. Nevertheless, one has to take into account that some of them have not been experimentally tested yet; therefore, the main properties of the material are a combination of the actual experimental and theoretical results as reviewed below:

2.2.1 Structural diversity. Antimonene presents many allotropic forms, creating a wide range of possibilities and tunability in terms of properties.⁸⁷ However, theoretical calculations have revealed that the only free-standing stable allotropes are the β and α allotropes. In this context, α and β allotropes of antimonene monolayers have been studied using DFT theory suggesting them as suitable materials for micro-electronic and optoelectronic nanodevices and solar cell applications (Fig. 6).⁸⁸

Nevertheless, the study of antimonene heterostructures revealed the plasticity of this novel material, the structure of which is critically dependent on its surroundings. This includes thickness driven phase transitions and substrate-layer stability dependence.^{82,83} This rich allotropic dynamism generates a

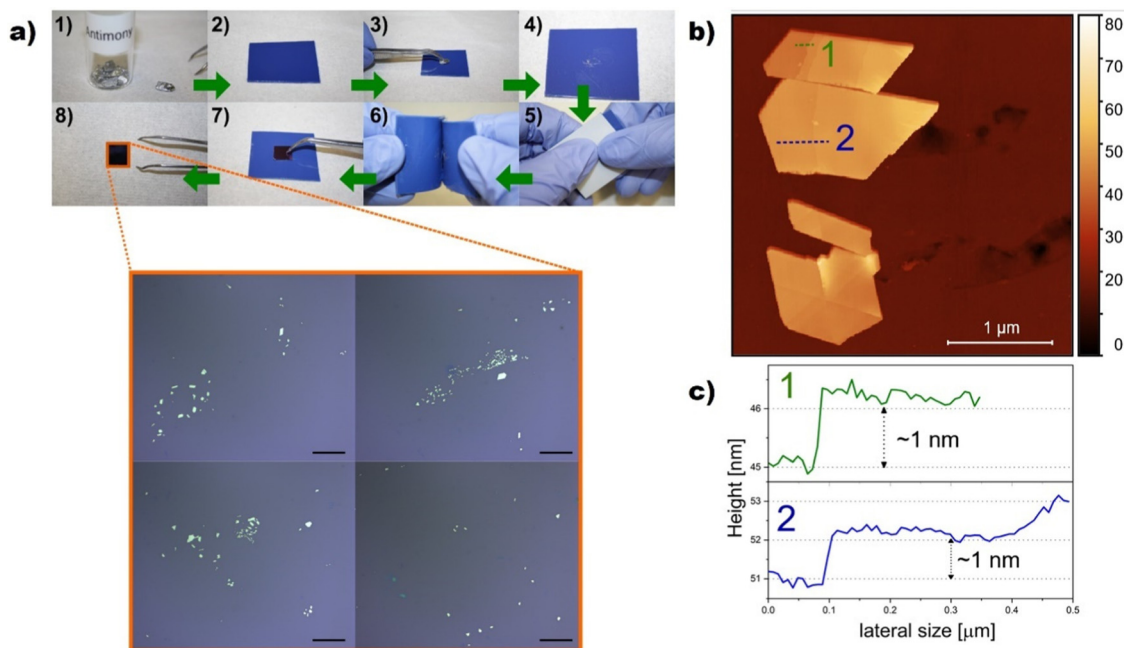
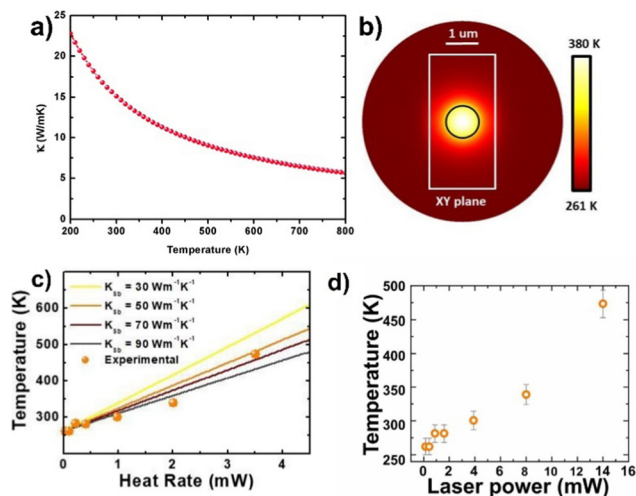


Fig. 7 (a) Step-by-step procedure (1–8) for the exfoliation of ANSs using micromechanical approach. Inset in (8) Optical micrographs showing exfoliated ANSs with different polygonal geometries. Scale bars 20 μ m. (b) AFM image of typical ANSs and (c) height profiles along the dashed lines showing steps of approximately 1 nm, compatible with a single layer antimonene. Adapted from ref. 98 with permission from IOP Publishing, copyright 2020.



Electrical transport in this material has also been recently studied, concluding that antimonene is expected to exhibit unusual transport properties due to its topological phase transition feature and quantum spin Hall edge states.⁹³ These intrinsically localized edge channels oriented to electrical transport can be controlled by applying an external electric field.⁹³

2.2.5 Thermal properties. The thermal properties of antimonene have been theoretically studied by Wang *et al.* using the Boltzmann transport equation, which revealed a low lattice thermal conductivity of $15.1 \text{ W m}^{-1} \text{ K}^{-1}$ at 300 K, thus demonstrating its potential applications for next-generation thermoelectric devices.^{95–97} This lattice thermal conductivity decreases with temperature, as expected for crystalline materials where phonon-phonon scattering rules the thermal conductivity in the high temperature range.⁹⁵ The low value at 300 K is related to the small group velocity, with low Debye temperature and large buckling height. Fig. 8(a) reflects the predicted lattice thermal conductivity of antimonene as a function of temperature. Experimentally, Fickert *et al.* studied the thermal and photothermal properties of antimonene nanosheets isolated on a SiO_2/Si substrate by micromechanical exfoliation.⁹⁸ Using a Raman spectroscopy-based thermometric measurement combined with numerical simulations of heat transfer, they estimated a thermal conductivity value of $90 \text{ W m}^{-1} \text{ K}^{-1}$ (Fig. 8(b) and (c)). A slight deviation of the estimated thermal



This journal is © The Royal Society of Chemistry 2023

2.2.8 Electrochemical properties. Concerning electrochemical properties, antimonene exhibits a pronounced reactivity in both aqueous and organic media. Indeed, electrochemical sodiation/desodiation processes yielded a pronounced anisotropic volume change along the *a/b*-axis and partially reversible crystalline-phase transformations ($\text{Sb} \rightarrow \text{NaSb} \rightarrow \text{Na}_3\text{Sb} \rightarrow \text{NaSb} \rightarrow \text{Sb}$), leading to a high theoretical capacity of 660 mA h g^{-1} .⁷⁴ On the other hand, performance of antimonene as a hydrogen evolution reaction (HER) electrocatalyst seems to be somehow related to the irreversible formation of superficial antimony oxides (with different oxidation states) during the electrochemical procedure, as well as the thickness and the number of edges in the antimonene flakes, which contribute to the formation of electroactive sites (*vide infra*).^{111,112} This work

3. Synthetic approaches in the preparation of antimonene and its heterostructures

3.1 Top-down approaches

The diagram illustrates two synthesis routes for Sb-based MXene nanosheets:

- Top-down route:** Starts with a bulk Sb-based MAX phase (labeled with Sb and 51). It is processed via **ME** (Mechanical Exfoliation) to produce a nanosheet. Alternatively, it is processed via **LPE** (Liquid Phase Exfoliation) and **EE** (Electrochemical Exfoliation) to produce a nanosheet. The LPE and EE steps are shown with a beaker containing a yellow liquid and a stirrer, with a lightning bolt symbol indicating electrochemical processes.
- Bottom-up route:** Starts with a collection of small particles. These are processed via **SPS** (Spark Plasma Sintering) to form a dense, hexagonal nanosheet. Alternatively, they are processed via **EG** (Electrochemical Growth) to form a nanosheet on a substrate.

distance between the layers in bulk antimony and the higher strength of the interlayer interactions, makes it extremely difficult to strip-off thin antimony layers using the conventional Scotch-tape approach. This micromechanical exfoliation starting from a freshly cleaved crystal of β -antimony was used in the first isolation of antimonene by Zamora *et al.*⁸⁴ Fig. 7 depicts the resulting antimonene nanosheets obtained from millimetre-sized crystals of antimony. Initially, they observed that the direct transfer of the sub-millimetre flakes obtained from peeling the bulk Sb to a SiO_2 substrate led to a very low transfer yield. This problem was overcome by adding an initial transfer from the Scotch tape to a thin layer of a viscoelastic polymer adhered to a glass slide. As a result, a higher yield of deposited flakes was observed that were then transferred to the SiO_2 substrate. With this modification in the deposition method, the authors reported the presence of few-layer and single-layer antimonene in a more controlled way.⁸⁴

The as-obtained micrometric-flakes were then easily identified by means of optical microscopy. Then, AFM images depicted an average height of *ca.* 0.9 nm for a monolayer terrace at the bottom of a few-layer antimonene flake (Fig. 10). As previously commented, the 0.9 nm value takes into account the existence of water molecules trapped between the flake and the SiO₂ substrate.^{85,86} Nevertheless, statistics has to be taken into account when talking about AFM thicknesses. The mechanical stability of the monolayer terrace was also confirmed after folding it with no breakage by AFM-assisted nanomanipulation. Additional techniques such as high-resolution transmission electron microscopy (HRTEM) and X-ray energy dispersive spectroscopy (XEDS) in combination with high-resolution AFM confirmed the quality of the material and its rhombohedral structure, that is, corresponding to β -antimonene. Finally, the stability of the material under ambient conditions as a function of time (up to two months) was also studied. It was observed that not only is antimonene stable after that time but also is after the immersion of the sample in water, thus depicting the high overall stability of the material in the presence of moisture (the role exerted by surface oxidation will be discussed later, *vide infra*).⁸⁴

Recently, our group managed to introduce a deterministic method to easily isolate antimonene nanosheets (ANSs) through an adapted micromechanical exfoliation approach using a high-tack adhesive film.⁹⁸ Indeed, we have been able to isolate ANSs exhibiting well-defined polygonal shapes with smooth surfaces and sharp edges (Fig. 10(e) and (j)) in very high density over the SiO₂/Si substrate. Topographic analysis using AFM revealed ANSs in a few-layer regime with thicknesses down to 14 nm (Fig. 10(f) and (g)). Moreover, the Raman spectra of the thin flakes displayed a noticeable blue-shift due to the strong electron–lattice interaction resulting from the reduced stacking order, which falls perfectly in line with previous theoretical predictions (Fig. 10(h)).¹¹⁷ Furthermore, we have been able to demonstrate a perfect correlation using four different analytical techniques, namely optical microscopy, AFM, scanning Raman microscopy (SRM) and scanning electron microscopy (Fig. 10(e), (f), (i) and (j)), respectively. This

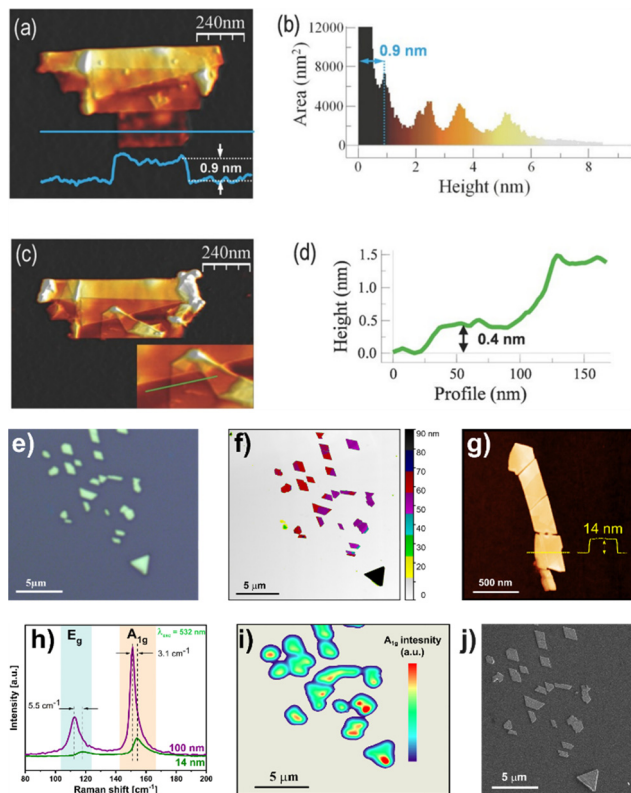


Fig. 10 AFM topography images of an antimonene flake with a monolayer terrace at the bottom. (a) AFM topography showing an antimonene flake with terraces of different heights. (b) Height histogram of the image in (a) pointing out the different thicknesses of the terraces. (c) Same flake as in (a) after a nanomanipulation process to confirm the stability of the material. The lower terrace of the flake was folded upward resulting in an origami structure with different folds. The inset corresponds to the area of the origami where the lowest step height is found. (d) Profile along the green line in the inset in (c). (e) Optical micrograph of a typical antimonene nanosheet isolated on SiO_2/Si substrate using micromechanical exfoliation. (f) False-colored AFM image of the same ANSs with incremental color code to highlight the terraces. Each color indicates a 10 nm step. (g) AFM image of a few-layer antimonene nanosheet and height profile along the dashed yellow line. (h) Comparative Raman spectra of the pristine bulk (100 nm) and few-layer (14 nm) antimonene nanosheets, remarking the blue shift of the $\text{A}_{1\text{g}}$ and E_{g} modes for the few-layer antimonene nanosheets. (i) Scanning Raman microscopy (SRM) map of the intensity of $\text{A}_{1\text{g}}$ mode of the flakes in (e). (j) Scanning electron microscope (SEM) image of the same flakes in (e). Adapted from ref. 84 with permission from John Wiley & Sons, copyright 2016, and ref. 98 with permission from IOP Publishing, copyright 2020.

neat correlation allowed for the simultaneous and at the same time unambiguous identification of the morphology and the chemical structure of the probed sample. It is worth noting that such correlations are of critical importance in the characterization of 2D materials, and the reliance on individual measurements in distinct locations, even within the same sample, can be dangerously misleading, especially for new and not well understood systems such as the case of antimonene. It is commonplace to encounter washing solvent residues or impurities from the polymer used for delamination exhibiting flat morphologies, which might be erroneously identified as

antimonene flakes if solely measured by AFM without a direct correlation to other techniques, such as Raman for instance.

The main limitation of this micromechanical approach is that it yields a low quantity of exfoliated material, highlighting the need for alternative methods to develop antimonene on a large scale.

3.1.2 Liquid phase exfoliation (LPE). This top-down approach is widely known for its successful use towards the delamination of bulk materials to produce their 2D counterparts in large quantities.^{49,118–120} From van der Waals materials such as graphene to ionic solids like layered double hydroxides, LPE allows the preparation of colloidal suspensions of the desired material in a wide variety of solvents. The family of pnictogens was not foreign to this method since phosphorene has been successfully isolated yielding relatively concentrated samples.⁵⁹ As thoroughly discussed by Backes *et al.*,¹²⁰ LPE methods are based on the solubility parameters (such as the surface tension or the Hansen and Hildebrand parameters) theory. In this context, the stabilization of the nanomaterial is achieved when the solubility parameters of both solvent and solute match. Some of the most typical solvents that give stable dispersions are the following: *N*-methyl-2-pyrrolidone (NMP), *N*-cyclohexyl-2-pyrrolidone (CHP), dimethylformamide (DMF), dimethyl sulfoxide (DMSO) and isopropyl alcohol (IPA). The overall procedure consists of three stages: first, the interlayer attraction between the material's sheets is overcome by supplying energy (*e.g.* with ultrasonic waves). Then, the as-obtained nanosheets are stabilized with suitable solvents preventing the reaggregation of the material. Finally, a size-selection procedure is often required because of the poly-dispersity of the dispersions.¹²⁰ Regarding antimonene, Abellán, Zamora *et al.* reported in 2016 the first LPE of few-layer antimonene.¹²¹ In that work, they report a fast and simple method to obtain highly stable IPA/ H_2O (4:1) suspensions of few-layer antimonene starting from bulk Sb crystals. Afterwards, the non-exfoliated material was removed by cascade centrifugation at 3000 rpm. To do this, the LPE process is carried out with tip sonication avoiding additional stabilizers such as surfactants. The high quality of the nanosheets was unveiled with AFM, scanning electron microscopy (SEM), Raman spectroscopy or EELS. AFM on SiO_2 substrates revealed step heights of 4 nm, related to the presence of few-layer material (Fig. 11). This value considers the overestimation because of residual solvent or additional contributions such as adhesion and capillary forces.^{59,122,123} The overall lateral dimensions were found to be in the 1–3 μm range and the atomic periodicity indicates a β -phase. Additionally, the obtained nanolayers were extremely stable under ambient conditions. Regarding the Raman characterization, the correlation of statistical Raman microscopy (SRM) with AFM in a polydisperse sample revealed antimonene flakes with thicknesses below 70 nm, corresponding to 17 layers, and barely showing any Raman signal. This result was similar to that observed for micromechanically exfoliated flakes.⁸⁴

After this initial work back in 2016, LPE is commonly being used as a methodology to obtain antimonene.^{112,124,125} Since



Fig. 11 (a) TEM image of FL antimonene nanolayers. (b) Representative topographic AFM image (scale bar 2 μm) of the exfoliated FL antimonene nanolayers. (c) Corresponding Raman A_{1g} map (scale bar 2 μm) of the exfoliated FL antimonene nanolayers contained in the area dotted in white in (b). (d) AFM image of typical ANS showing polydisperse nanosheets exfoliated by ultrasonication. (e) Statistical dispersion of ANS lateral size as a function of thickness. (f) Thickness measured by AFM along the lines numbered in (d). Adapted from ref. 112 with permission from Royal Society of Chemistry, copyright 2019, and ref. 125 with permission from IOP Publishing, copyright 2020.

then, great effort has been made to maximize the concentration of the samples obtained by LPE, while maintaining an appropriate “dimensional anisotropy” (DA) ratio, which has been defined as the ratio between the height and length of the nanolayers, providing a good estimation of the morphology of the nanolayers (having the thin and large flakes a high DA ratio). We have reported a systematic study of the exfoliation process of antimony bulk crystals, with the aim to obtain stable FL antimonene suspensions with a high nanolayer concentration as well as a high DA ratio, by optimizing different parameters of the exfoliation procedure.¹¹² Specifically, the results show that the pre-processing of the material using wet-ball milling with 2-butanol strongly affects both the concentration and morphology of the suspension of FL antimonene. Moreover, the analysis of 28 different solvents previously selected based on Hansen parameters as well as other experimental observations yielded the highest concentration of FL antimonene for the mixture of NMP/H₂O in a (4 : 1) ratio, *ca.* 0.368 g L⁻¹ (~yield of 37 wt%), while the largest DA value was obtained using 2-butanol (*ca.* 27.6). The nanolayer heights was comprised between 2 and 8 nm and lateral dimensions lower than *ca.* 300 nm. Additionally, this work revealed that using tip sonication employing an ultrasonic wave amplitude of 100% yields better results in terms of DA than bath sonication. Interestingly, the use of 2-butanol also yielded a large number of edges and electroactive sites that strongly influence the electrochemical behavior of the exfoliated antimonene, forming also irreversible superficial antimony oxides.¹¹²

A particular case within the LPE is that of the antimonene quantum dots (AMQD). This type of material – of great interest in biomedical applications (*vide infra*) – which is characterized by lateral dimensions < 8 nm, is obtained after subjecting the

bulk antimony samples to an iterative sonication and centrifugation process for long periods of time using high power and high amplitude values.^{126,127} More in detail, this procedure combines ultrasound tip sonication with ice bath sonication of bulk Sb in NMP or ethanol, followed by a low-speed centrifugation to remove the larger particles and a high-speed centrifugation to isolate the desired QD particles. Fig. 12 highlights the synthesis and characterization of AMQDs in EtOH according to ref. 127. The resulting solution displays a high yield in the synthesis of uniform and small particles with average size and thickness of *ca.* 3 and 2 nm, respectively, as detected by AFM, in good agreement with TEM images. The composition of the AMQDs and the presence of Sb was determined *via* XPS and Raman spectroscopy. Moreover, in order to improve their biocompatibility, a non-covalent functionalization with polyethylene glycol (PEG) moieties has been carried out.

The as-obtained PEG-coated AMQDs exhibited excellent stability in physiological experiments; no signs of toxicity in cells in the studied range of concentrations and excellent photothermal conversion efficiency upon NIR irradiation. Beyond the biomedical applications,¹²⁷ recent studies on AMQDs points to them as promising candidates in optoelectronic devices, and more specifically in quantum-dot-sensitized solar cells.^{128,129} In this sense, the work of Zhang *et al.*¹²⁹ presents liquid phase-synthesized AMQDs as an effective photoactive material in quantum-dot-sensitized solar cells. The AMQDs were prepared following the aforementioned protocol starting from bulk Sb crystals using a simple probe ultrasonic procedure followed by an ultrasound bath treatment. The temperature during the probe sonication was set under 25 °C to avoid possible oxidation or degradation processes. Afterwards, the dispersion was centrifuged to remove the residual Sb bulk particles and the resulting suspension was centrifuged at high speed (12 000 rpm) to collect the supernatant AMQDs, which were re-suspended in NMP. AFM

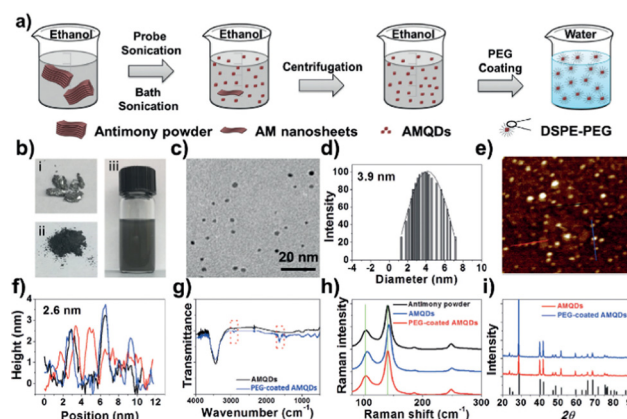
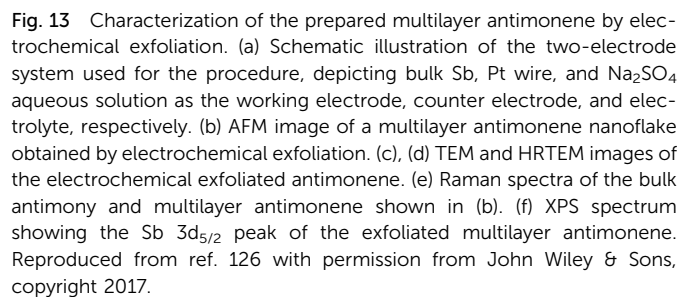


Fig. 12 (a) Fabrication of PEG-coated AMQDs. (b) Images of bulk antimony, antimony powder, and AMQD solution during the preparation process. (c) TEM image, (d) diameter distribution, (e) AFM image, and (f) thickness of the PEG-coated AMQDs. (g) FTIR spectrum, (h) Raman spectrum, and (i) XRD spectrum of AMQDs and PEG-coated AMQDs. Reproduced from ref. 127 with permission from John Wiley & Sons, copyright 2017.

The ability to intercalate alkali metals shown by Sb allows the formation of antimony intercalation compounds to be envisioned, in analogy to previously reported black phosphorus intercalation compounds (BPICs), which under appropriate solvents and under thorough exclusion of oxygen and water may lead to pnictogenide dispersions.^{61,134–136}

The MBE approach was previously carried out by Lei *et al.* with the growth of single layer Bi (111) on Bi₂Te₃ (111) and Bi₂Te₃ (111) substrates with a small lattice mismatch.¹³⁹ Afterwards, Wu *et al.* were able to grow antimonene monolayers (thickness of *ca.* 0.28 nm as measured by the profile line across the edge of the antimonene film) on PdTe₂ substrates



(Fig. 14).¹⁴⁰ In that work, both *in situ* low-energy electron diffraction (LEED) and scanning tunneling microscopy (STM) measurements confirmed the high quality of the epitaxially-grown antimonene with a honeycomb graphene-like structure. XPS results reported that the interaction between antimonene and the substrate is *via* weak van der Waals forces. The combined results of STM and XPS highlighted a good stability of the material against air exposure for 20 min.

Most recently, additional studies have used MBE to grow antimonene on Ge (111) and Ag (111) (Fig. 14) substrates, confirming the weak interactions between the monolayer and the substrate as well as the honeycomb structure.^{81,141}

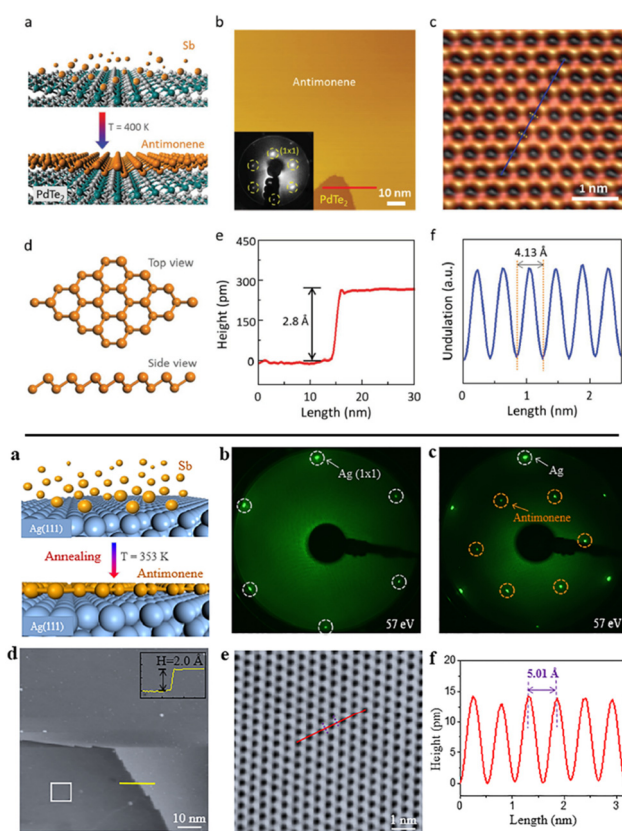


Fig. 14 Top: (a) Schematic of fabrication of an antimonene monolayer formed on the PdTe_2 substrate obtained by MBE approach. (b) STM topographic image of large antimonene island on PdTe_2 . (Inset: LEED pattern of antimonene on PdTe_2 .) (c) Atomic resolution STM image of monolayer antimonene showing the graphene-like honeycomb structure. (d) Top view and side view of the buckled conformation of the antimonene honeycomb. (e) Height profile along the red line in (b), showing that the apparent height of the antimonene island is 2.8 Å. (f) Line profile corresponding to the blue line in (b), revealing the periodicity of the antimonene lattice (4.13 ± 0.02 Å). Bottom: (a) Schematic of the MBE fabrication process. (b) LEED pattern of a clean $\text{Ag}(111)$ substrate. (c) LEED pattern of antimonene on $\text{Ag}(111)$. (d) Large scale STM image of monolayer antimonene on the $\text{Ag}(111)$ (inset: height profile along the yellow line at the terrace edge). (e) High-resolution STM image of antimonene depicted by the white square in (d). (f) Line profile corresponding to the red line in (e), revealing the periodicity of the antimonene lattice (5.01 Å). Adapted from ref. 140 with permission from John Wiley & Sons, copyright 2016, and ref. 141 with permission from American Chemical Society, copyright 2018.

Moreover, these studies revealed a semi metallic behavior for a single layer of deposited antimonene. MBE has also been reported to obtain multilayer antimonene nanoribbons on sapphire substrates that can extend themselves to a length of few microns.³⁶ These ribbons were grown *via in situ* thermal annealing after the initial MBE deposition. Their formation mechanism, supported on SEM and AFM measurements, considers an adatom migration process at an elevated temperature in combination with strain relaxation and surface energy balance.

vdWE is based on the use of substrates with the absence of dangling bonds on their surface. Thus, the epitaxially grown layer of the layered material is connected to the substrate by means of weak van der Waals interactions in the absence of strong chemical bonds. Therefore, it is possible for the material to exhibit a different crystalline symmetry than that of the substrate. The first few-layer antimonene grown by vdWE was reported in 2016 by Ji *et al.*¹¹⁷ Fig. 15 highlights the antimonene layer synthesized on mica substrates by means of a van der Waals epitaxy.

In that work the high-quality synthesis of few-layer antimonene with a buckled hexagonal structure (β -phase) was reported as confirmed by HRTEM and Raman spectroscopy. This finding is consistent with the predicted as most stable allotrope of monolayered antimonene. In broad strokes, the synthesis is carried out in a two-zone tube furnace with separated temperature controls. The bulk Sb is placed in one of the regions and then heated to obtain Sb vapor. A transport flow of $\text{Ar} + \text{H}_2$ transfers the Sb vapor to the other region of the furnace, in which there is a substrate at a lower temperature than the first region, hence promoting the condensation of Sb. The high stability of the material and an average dimension (5–10 μm) and thicknesses (*ca.* 4 nm, *i.e.*, few-layers) were analysed by optical microscopy, AFM, Raman spectroscopy and XPS. The

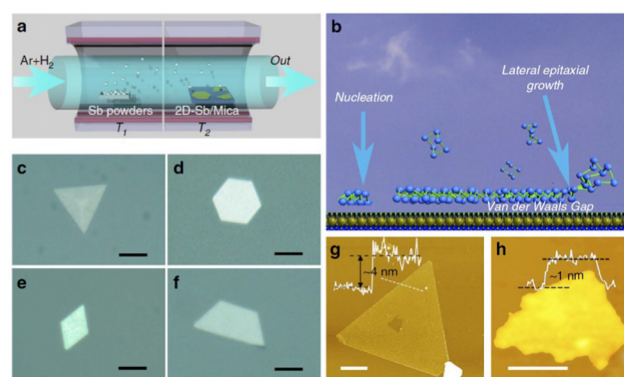


Fig. 15 Antimonene synthesized on mica substrates *via* vdW epitaxy. (a) Schematic illustration of the sample synthesis configurations. (b) Schematic diagram of the vdWE. (c)–(f) Optical images of typical antimonene polygons with triangular, hexagonal, rhombic, and trapezoidal shapes, respectively. The scale bar is 5 mm. (g) AFM image of a typical triangular antimonene sheet. The scale bar is 1 mm. (h) AFM image of a tiny antimonene sheet with a thickness of *ca.* 1 nm. The scale bar is 50 nm. Reproduced from ref. 117 with permission from Springer Nature, copyright 2016.



stability of the nanosheets was tested with an as-prepared and a 30 day aging sample, with no additional signature in the corresponding Raman spectra or X-ray energy-dispersive spectroscopy (XEDS). The good electrical conductivity of the synthesized antimonene (10^4 S m^{-1}) in combination with the wavelength independent high transparency in the visible light spectrum endows this material with potential applications as a flexible transparent electrode.¹¹⁷

Along this front, Hogan *et al.* reported the temperature-induced phase transition between α and β phases of antimonene in a van der Waals heterostructure on Bi_2Se_3 .¹⁴² The Bi_2Se_3 surface was prepared *via* an ultra-high vacuum chamber, and the antimony was then sublimated and deposited at room temperature. Once antimony is deposited, it forms α -antimonene domains with different orientations with respect to the substrate. However, after mild annealing at 473 K, there is a growing of the β phase that overcomes α -antimonene, leading finally to a single domain of β -antimonene which exactly matches with the surface lattice structure of Bi_2Se_3 . These results were also supported by DFT calculations, which highlight the lattice matching of the β in stark contrast with the α one.

Last but not least, recent studies using vdWE have demonstrated the experimental synthesis of antimonene-based vdW heterostructures, proving the stability of both the hexagonal β - and rectangular α -forms of antimonene, on top of the topological insulator α -bismuthene.¹⁴³ Moreover, these studies have allowed the elucidation of the rich allotropic/polymorphic structural diversity of antimonene, revealing extremely interesting rotational vdW epitaxy in 2D Sb/graphene heterostructures. Furthermore, thanks to these novel heterostructures several aspects related to the dynamic oxidation and phase transition of antimonene have been corroborated. These interesting points will be further analyzed below.

3.2.2 Solution-phase synthesis. One of the most promising bottom-up approaches has been reported by Peng *et al.* using a solution-phase synthesis of few-layer antimonene *via* anisotropic growth.¹⁴⁴ This work addresses the fact that the actual synthetic methods for obtaining high-quality few-layer antimonene nanosheets (exfoliation and epitaxial growth) have hindered the large-scale production of this material. The authors propose the direct synthesis of few-layer and promoting their anisotropic growth in a colloidal solution, starting from SbCl_3 , together with oleylamine and dodecanthiol. While oleylamine is employed as the reducing agent to obtain $\text{Sb}(0)$, dodecanthiol is used to prevent the formation of oxides. In this synthesis the role of the chloride anions is crucial to induce the hexagonal final form. Fig. 16 depicts how the final morphology of the resulting antimony species can be tuned if some experimental parameters are modified during the synthesis. The same authors recently reported further insights into the formation of hexagonal antimonene as well as remarked on the role of the chloride salt (SbCl_3) as a key factor in the resulting morphology. Furthermore, they replace the use of dodecanthiol by alkyl phosphonic acids to avoid the presence of sulphur-side products.¹⁴⁵

Some of the advantages of the solution-phase methodologies rely on their simple procedures, together with the

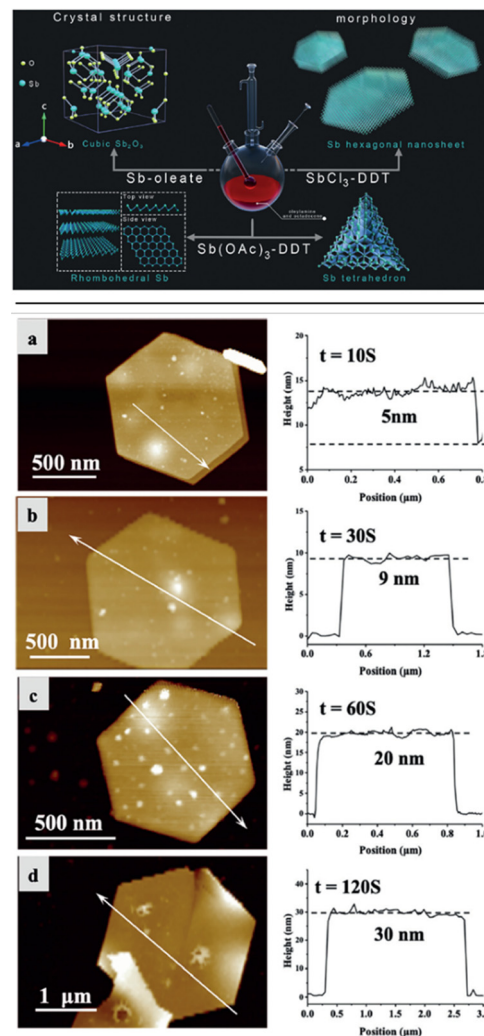
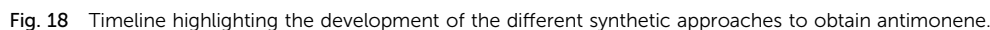
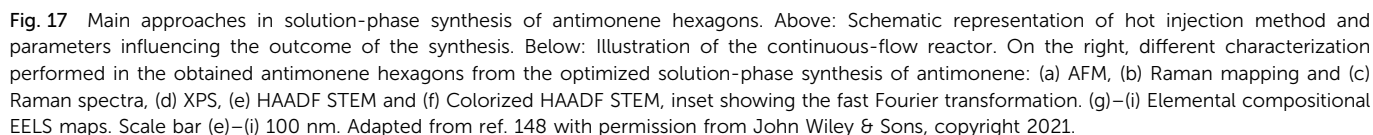


Fig. 16 Top: Illustration of the wet chemical solution-phase synthesis of antimony trioxide, antimony tetrahedral, and hexagonal antimonene nanosheets from Sb-oleate, $\text{Sb}(\text{OAc})_3$ -DDT, and SbCl_3 -DDT as precursors, respectively. Bottom: AFM images and the corresponding height profiles of hexagonal antimonene nanosheets with tunable layer thicknesses obtained at different annealing times at 300 °C: (a) 10 s, (b) 30 s, (c) 60 s, and (d) 120 s. Reproduced from ref. 144 with permission from John Wiley & Sons, copyright 2019.

tunability of the material from the point of view of size, morphology and composition, as well as the monodisperse character of the obtained samples,^{146,147} opening the door to the large-scale synthesis of the desired material. Indeed, the authors modulated to some extent the average thickness of the nanosheets by tuning the annealing time. They characterized the nanosheets *via* Raman spectroscopy, TEM and XRD proving that the material consisted of β -antimonene. Furthermore, X-ray photoelectron spectroscopy (XPS) results confirmed the presence of chloride anions on the surface of the antimonene, as well as the coordination of dodecanthiol, thus suggesting surface functionalization.

Furthermore, the colloidal synthesis of antimonene has been very recently studied by Abellán, Zamora and co-workers, optimizing the different synthetic parameters to





To sum up, Fig. 18 and Table 3 expose an historical timeline and general overview of the main synthetic approaches developed for antimonene, highlighting the main aspects associated with each of them.

Regarding the most typical characterization techniques to confirm the identity of antimonene, there are the following:

This journal is © The Royal Society of Chemistry 2023

	Synthetic approach	Main aspects	Ref.
Top-down	Micromechanical exfoliation	<ul style="list-style-type: none"> • First isolation of few and single-layer antimonene • Milimeter-sized crystals • Easy identification (optical microscopy) • Low quantity of exfoliated material, time consuming, irregular morphology and lack of homogeneity in exfoliation. 	First time reported: ⁸⁴ Other works: ¹⁴⁹
	Liquid phase exfoliation	<ul style="list-style-type: none"> • Suspensions of the material in adequate solvents (NMP, DMF, and IPA...) • Based on solubility parameters • Size selection (cascade centrifugation) • Micrometer-sized crystals of few-layer antimonene (AFM) • Irregular morphology and polydispersity. 	First time reported: ¹²¹ Other works: ^{112,124,125,150}
	Electrochemical exfoliation	<ul style="list-style-type: none"> • Two-electrode cell • Electrolyte solution containing few-layer antimonene dispersion. • Size selection (cascade centrifugation) • Micrometer-sized crystals of few-layer antimonene (AFM) • Irregular morphology and polydispersity. 	First time reported: ¹²⁶ Other works: ^{107,151}
	Pressurized alloy assisted synthesis	<ul style="list-style-type: none"> • Uses pressure created from the protonation of the alloy, creating a buoyancy that exfoliates antimonene • Irregular morphology, wide size distribution, but very thin flakes (1–2 nm) 	First time reported: ¹³³
Bottom-up	Epitaxial growth	<ul style="list-style-type: none"> • Molecular beam epitaxy (MBE) and van der Waals epitaxy (vdWE) 	First time reported: MBE, ¹⁴⁰ vdWE ¹¹⁷ Other works: ^{81,108,141,142,152–155}
	Solution-phase synthesis	<ul style="list-style-type: none"> • Used to grow antimonene on substrates (mica, Ge(111), Ag(111)...) • Micrometer-sized crystals of single-layer antimonene (AFM) • Irregular morphology, low quantity if the material and polydispersity. • Based on the anisotropic growth of antimonene • Large-scale production of the material • Micrometer-sized crystals of few-layer well-defined hexagonal antimonene (AFM) • Polydispersity 	First time reported: ¹⁴⁴ Other works: ^{145,148}

Electron microscopy provides the morphology of the material and is revealed as a key technique in the search for a desired morphology, such as well-defined hexagonal samples in solution phase synthesis or the AMQDs.^{127,144} Even though TEM, HRTEM or SEM cannot be used to analyse the thickness of the sample, they can be used for measuring the average lateral dimension as well as taking wider areas of the deposited material throughout the whole substrate. In this context, aberration-corrected scanning transmission electron microscopy (STEM) combined with EELS can be used to investigate the local structure and chemistry of the flakes (Fig. 19–21). For example, for LPE samples, high-angle annular dark-field images taken at low voltages to prevent damaging the flakes highlight the atomic-resolution of the crystal structure, confirming a β -phase as well as the good crystallinity and the absence of defects in the studied antimonene flakes. The EEL

Further studies about antimonene/graphene heterostructures have been carried out by Bayer *et al*, where they studied the allotropic phases of antimonene grown by vdWE onto CVD graphene. They found the coexistence of two main morphologies: 2D rhombohedral β -antimonene, and a one-dimensional nanowire structure with rectangular basis.⁸³ Remarkably, both morphologies exhibit direct in-plane rotational vdW epitaxy with the graphene support. These results open the door for the scalable production of antimonene heterostructures by bottom-up approaches.

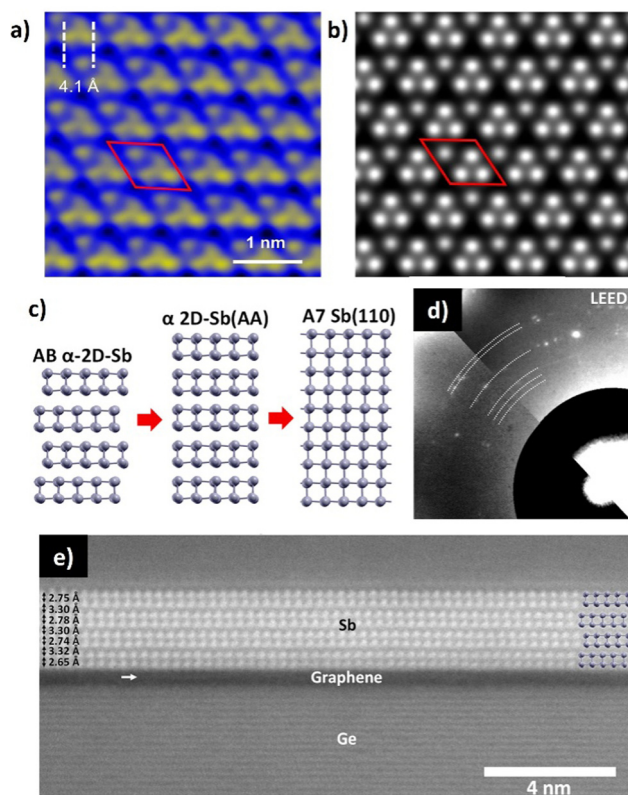


Fig. 19 (a) Atomically resolved STM image of an antimonene monolayer on SbAg_2 surface alloy on $\text{Ag}(111)$. (b) The simulated STM in the constant height mode (~ 2 Å). (c) Schematic representation of the layer-dependent A17 (AB α -2D-Sb) transition to A7 in antimonene. (d) LEED pattern of 2D-Sb on graphene. Part of the Ewald sphere at 44 eV is shown in the bottom left and at 29 eV is shown in the top right. (e) STEM of a cross section of 4 bilayers A17 antimonene island on graphene. Adapted from ref. 82 and 152 with permission from American Chemical Society, copyright 2020.

As in other 2D materials prepared using top-down approaches, XRD is one of the most commonly used techniques because it can confirm the diffraction patterns of the resulting product allowing identification of the antimonene crystalline phase.^{112,144} In this context, bulk Sb and antimonene exhibit very similar XRD patterns. The main difference relies on the weaker intensity of the (003) and (006) peaks located at *ca.* 23.7° and 48.5° , respectively, of the antimonene compared with that of bulk Sb.¹⁵⁸ This effect is indicative of the reduction of the antimony crystals along the *c*-axis mainly.¹²⁴ The rhombohedral phase of Sb is indexed as PDF#035-0732.¹⁵⁹ Fig. 20(a) depicts XRD patterns of bulk Sb, Sb micro-crystals after ball-milling and antimonene.

Raman spectroscopy is a powerful technique widely used to characterize 2D materials.^{59,160} The Raman spectrum of bulk Sb when excited at 532 nm depicts two main phonon peaks: A_{1g} and E_g modes at 149.8 and 110 cm^{-1} , respectively, and related to the in-plane and out-of-plane vibrational modes.¹⁶¹ Few-layer antimonene displays a shift in both bands to a higher wavenumber region (also called blueshift). In this sense, it is reported that the correlation of AFM with SRM¹⁶² indicated that antimonene samples with a thickness below

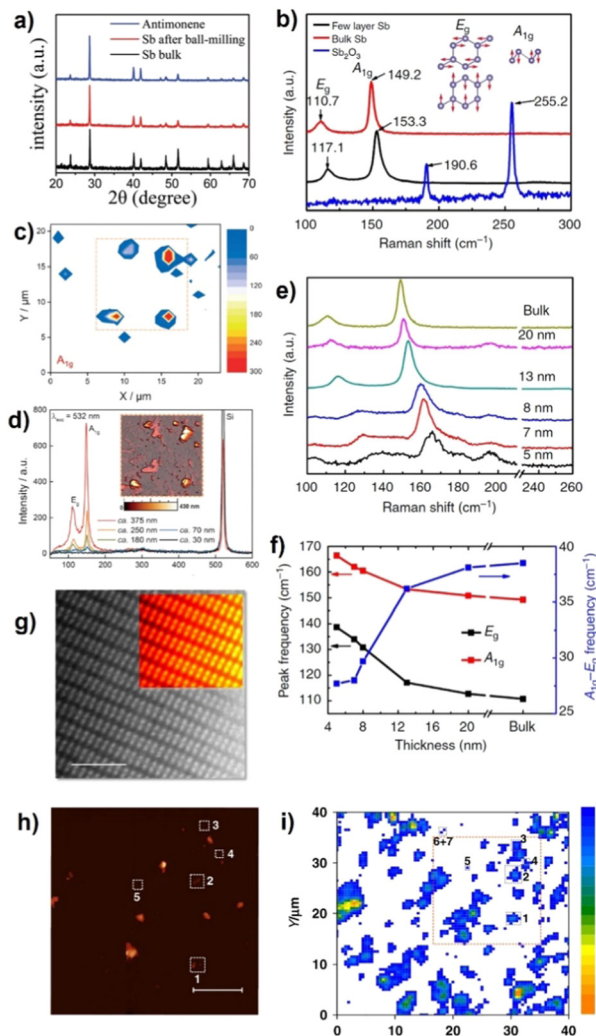


Fig. 20 (a) X-ray diffraction (XRD) patterns of bulk antimony crystals, antimony plates after ball-milling and antimonene. (b) Raman spectra of bulk antimony (β -phase), few-layer antimonene and antimony trioxide. Inset: Vibrational modes of β -phase antimonene. (c) A_{1g} intensity Raman mapping of solvent-exfoliated flakes deposited on a SiO_2/Si substrate. (d) Single-point Raman spectra measured at different thicknesses according to the topographic AFM image (inset) of the same area studied in (c) (dashed lines). (e) Raman spectra of antimonene polygons with different thicknesses, from 5 nm to bulk. (f) A_{1g} , E_g peak frequencies and energy difference of those two peaks plotted against sample thickness. (g) Atomic resolution HAADF image acquired on the edge of a free-standing portion of an antimonene flake obtained by LPE. The scale bar is 2 nm. (h) Representative AFM topography image (scale bar 5 μm) of exfoliated antimonene onto SiO_2/Si substrates. (i) The corresponding Raman A_{1g} mapping of the same antimonene flakes in (h). Adapted from ref. 65 and 117 with permission from Springer Nature, copyright 2019 and 2016, ref. 121 with permission from John Wiley & Sons, copyright 2016, and ref. 158 with permission from the Royal Society of Chemistry, copyright 2020.

70 nm (*ca.* 17 layers) barely show any Raman signal (Fig. 20(b) and (c)).¹²¹ Nevertheless, taking single-point spectra at different points of the sample does evidence how the peak intensities decrease concomitantly with the thickness of antimonene (Fig. 20(d)).¹²¹ It is worth noting that these Raman results follow the same trends independently of the synthetic



approach to obtain antimonene. The work of Ji *et al.*¹¹⁷ clearly illustrates how the Raman peaks of bulk Sb evolve after obtaining its layered counterpart and also compares the fingerprint for a Sb_2O_3 species, which exhibits a completely different pattern (Fig. 20(b)). Indeed, Fig. 20(e) shows the Raman spectra of antimonene polygons synthesized by vdW epitaxy with thicknesses varying from 5 nm to bulk. Moreover, Fig. 19(f) shows the A_{1g} , E_g peak frequencies (left vertical axis) and the energy difference (right vertical axis) of those two peaks plotted against sample thickness, confirming the blueshift observed in LPE samples. These sorts of blueshifts have been also reported for other 2D materials and are probably attributed to the fact that lattice constant shrinks when the number of layers decreases.^{163,164} Last but not least, by performing the LPE under inert conditions using bmim- BF_4 ionic liquid and argon-filled gloveboxes it is possible to obtain highly crystalline Sb nanosheets (Fig. 20(g)) that exhibit observable Raman signals with perfect AFM spatial correlation under environmental conditions down to the 5 nm limit, well below the previous LPE results using IPA/ H_2O mixtures (Fig. 20(h) and (i)).^{65,117} XPS analysis is an effective technique to study the oxidation state of the Sb atom as well as the surface oxidation state. In this sense, and due to the importance of this point, a thorough discussion is carried out in the following section.

4.1 Oxidation behaviour

As previously commented, it is reported that antimonene exhibits good structural integrity as well as high thermodynamic stability, even though theoretical studies predicted a high tendency for oxidation surpassing even that of phosphorene.⁶⁵ This is in good agreement with the recent experimental results in which O is always detected on the surface of the antimonene sheets.^{111,117,121} It is believed that the oxidation of antimonene leads to a surface oxidation layer that acts as a passivation coating, thus protecting the material from further structural decomposition.⁶⁰ This oxidation layer might potentially alter the final properties of the material, and eventually affect the associated applications.¹⁶⁵ Therefore, understanding the oxidation behaviour of antimonene from the fundamental viewpoint as well as from the experimental perspective is imperative for the future development of antimonene-based technologies. Recently, Assebban *et al.* published a seminal work comprehensively investigating the surface oxidation of liquid-phase exfoliated antimonene nanosheets (ANS).¹²⁵ First, they observed that the Raman spectra of the exfoliated ANNs featured, besides the typical vibrational modes at A_{1g} (149.8 cm^{-1}) and E_g (110 cm^{-1}), additional peaks at 190.5 and 254.6 cm^{-1} that were ascribed to Sb_2O_3 (Fig. 21).

Further STEM analysis combined with EELS elemental mappings has shown the formation of an amorphous layer rich in Sb and O, exclusively at the top surface and edges, which corroborated the observed partial oxidation caused by the sonochemical processing in IPA/ H_2O during exfoliation. The authors decided afterwards to submit exfoliated samples to thermal annealing at $210\text{ }^\circ\text{C}$ under ultra-high vacuum (UHV),

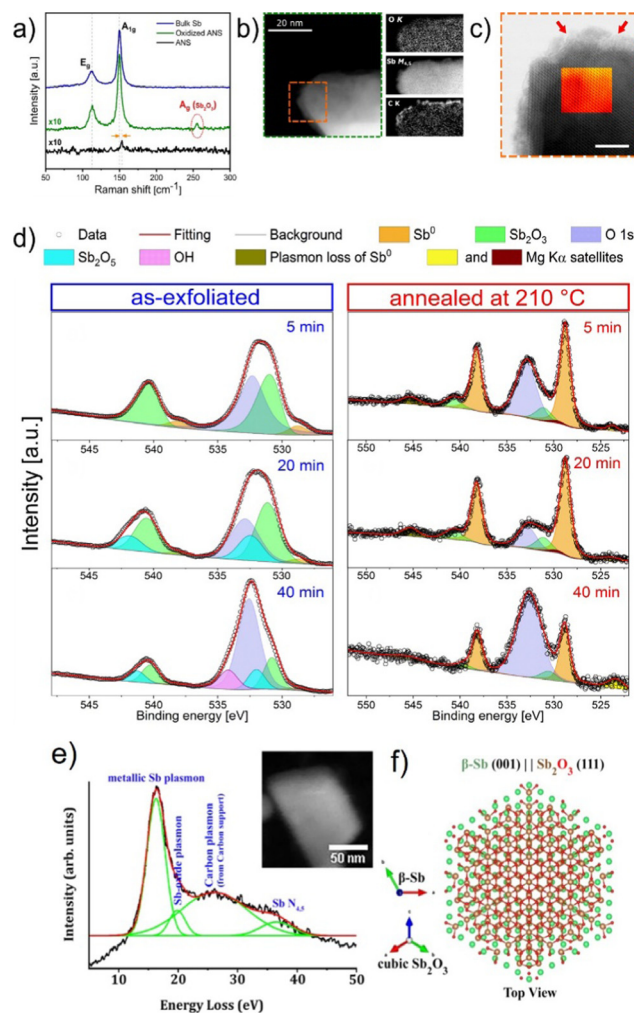


Fig. 21 (a) Raman spectra of bulk antimony, exfoliated ANS and oxidized-ANS exhibiting Sb_2O_3 Raman fingerprint at 254.6 cm^{-1} . (b) HAADF image of sub-nanometric ANS acquired at 80 kV and the corresponding elemental compositional maps derived from EELS. (c) High-magnification annular bright field (ABF) image near the edge of the nanosheet displayed in (b) (orange-dashed area) (scale bar 5 nm). (d) XPS line spectra in the Sb 3d region for antimonene nanosheet samples, as-exfoliated (left column) and after thermal annealing at $210\text{ }^\circ\text{C}$ under high vacuum (right column). (e) VEELS spectrum of the $\beta\text{-Sb}(001)$ crystal on suspended graphene (ADF STEM in the inset). Spectrum acquired after ~ 8 months ambient air exposure of the sample. (f) Atomic model of the suggested $\text{Sb}_2\text{O}_3(111)$ formed from ambient air exposure on $\beta\text{-Sb}(001)$ crystals. Adapted from ref. 83 with permission from Springer Nature, copyright 2021, and ref. 125 with permission from IOP Publishing, copyright 2020.

while tracking the surface chemistry using X-ray photoelectron spectroscopy (Fig. 21). They discovered that the thermal annealing resulted, to some extent, in the removal of previously observed surface oxide adlayer, as indicated by the *in situ* XPS evidence. More interestingly, by means of ultraviolet photoelectron spectroscopy (UPS), they demonstrated a change in the surface electronic properties, which upon annealing, switches from a metallic to an otherwise semiconducting material with an estimated band gap of approximately 1 eV, assuming the Fermi level is situated in the middle of the gap.



Bayer *et al.* also studied the oxidation behavior in PVD grown antimonene/graphene heterostructures by Valence EELS (VEELS), allowing any trace of surface oxidation to be precisely detected. VEELS revealed low levels of oxidation after 8 months of ambient exposure (Fig. 21(e)), and together with the ADF STEM FT patterns, revealed the presence of a sixfold structure that can be associated with cubic $\text{Sb}_2\text{O}_3(111)$. From these results, they suggest the formation of a thin crystalline layer of Sb_2O_3 on top of β -antimonene (Fig. 21(f)). These results again support the spontaneous formation of a 2D surface oxidation layer that passivates the structure of antimonene endowing the material with an outstanding environmental stability.^{83,166} This technique allows both spatial and chemical resolution of the surface of the flakes to be obtained with great precision. In particular, the XPS data of the flakes revealed the presence of an oxidation layer with a binding energy (BE; 530.9 eV) larger than the value expected for Sb_2O_3 (530 eV) and slightly higher than the value expected for Sb_2O_5 (530.8 eV). The O_2 peak also presented a higher BE value (532.61 eV) compared to most of the metallic oxides (531–528 eV), thus pointing to a superficial oxidized component present only on the outer surface and not presenting a conventional oxidation pattern. These results collected in 2017 by Abellán *et al.* already pointed to the spontaneous formation of antimonene oxides and suggested an explanation for the great stability of antimonene under environmental conditions.

Along this front, an experiment that has been key to understanding this behavior has been the one developed by Lloret *et al.* using highly concentrated bmim- BF_4 exfoliated

antimonene suspensions investigated by XPS. As can be observed in Fig. 22, next to the broad O 1s signal at 533 eV from the surface enriched ionic liquid contamination, the Sb 3d region between 525 and 545 eV of the FL- Sb_{SUS} sample (Fig. 22 right, spectrum II) reveals very weak Sb 3d_{3/2,5/2} signals from Sb in oxidation state zero at 528.2 eV for the 3d_{5/2} level, along with minor contributions from Sb in the higher oxidation state at around 530.3 eV. Removing most of the excess IL by heating in ultra-high vacuum clearly showed Sb signals originating mostly from bulk antimony zero (spectrum III). Finally, exposing the heated FL- Sb_{SUS} sample without the protecting IL medium for several hours in air led to a significant decrease in Sb(0) and concomitant increase of the oxidized Sb species (spectrum IV); these findings thus demonstrate the role of bmim- BF_4 in stabilizing the antimonene against oxidation, and more importantly, demonstrate the reactive nature of LPE antimonene with a pronounced oxophilicity. These findings are of uttermost importance as they first confirm the passivation of the antimonene surface by an oxide layer that shields it from further structural degradation, thus explaining the high stability of antimonene in comparison to its counterpart black phosphorus.¹⁶⁷ Second, they demonstrated a novel modification approach to tailor its properties by opening a bandgap. In the same context, and by means of first-principles calculations, Zhang *et al.* presented a new class of two-dimensional structures of antimonene oxide. These theoretical predictions are based on a monolayer antimonene with $\text{Sb}=\text{O}$ double bonds perpendicular to the antimonene plane [type (I) structure], and depending on the oxygen content, tunable direct

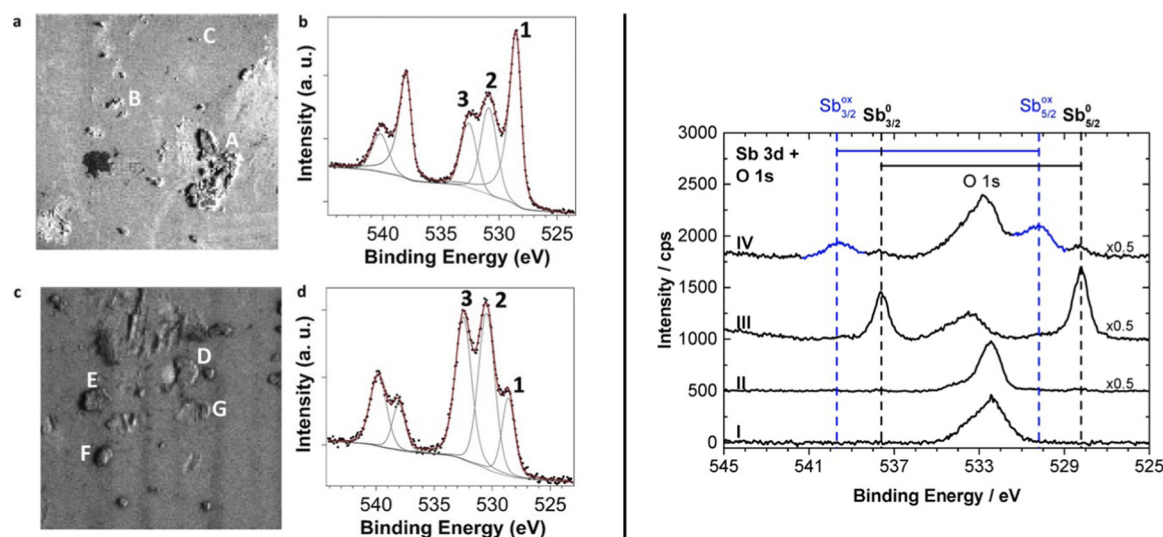


Fig. 22 Left: (a) Sb 3d image for the reference sample. Letters refer to the antimonene flakes studied. (b) Sb 3d peak for the reference sample, corresponding to point B in (a). Numbers identify the different components: 1 ($\text{Sb } 3d_{5/2}$), 2 (oxidized $\text{Sb } 3d_{5/2}$), and 3 ($\text{O } 1s$). Peaks at higher BEs are the $\text{Sb } 3d_{3/2}$ components. (c) The Sb 3d image for the functionalized antimonene. (d) Sb 3d peak for the functionalized sample, corresponding to point E in (c). The peak identification and other details are as in (b). The size of images in (a) and (c) is $40 \times 40 \mu\text{m}$. Right: XPS Sb 3d and O 1s region of the neat bmim- BF_4 IL (I) showing oxygen signals from the IL surface contamination layer, of the highly-concentrated FL- Sb_{SUS} suspension (II) showing small signals of non-oxidized ($\text{Sb } 3d_{5/2}$ at 528.2 eV) and minor contributions from oxidized (530.3 eV) antimony next to the oxygen contamination, after removal of most of the IL by heating in UHV (III), and after submitting the sample to environmental conditions for a day, showing a drastic decrease in Sb(0). Adapted from ref. 65 with permission from Springer Nature, copyright 2019, and ref. 165 with permission from John Wiley & Sons, copyright 2017.

bandgaps ranging from 0 to 2.28 eV have been calculated.¹⁶⁵ Later on, Wolff *et al.* realized that the fully oxidized antimonene monolayers presented by Zhang *et al.* are metastable and likely undergo a transition into a more stable configuration.¹⁶⁸ Based on density functional theory (DFT) calculations, they proposed a novel type of 2D antimony oxide single- and few-layer structures in which the oxygen atom is incorporated into the antimonene planes and is bound to at least two antimony atoms (Sb–O–Sb) [type (II) structure] (Fig. 23). They have also found out that, depending on stoichiometry and the type of bonding, the proposed 2D layers exhibit different structural stability and electronic properties, ranging from topological insulators to semiconductors with direct and indirect band gaps between 2.0 and 4.9 eV. More interestingly, they foresaw that semimetallic few-layer antimonene can naturally form heterostructures with semiconducting oxidized layers, and they have presented the corresponding vibrational modes, which agree with the experimental findings on liquid-phase exfoliated few-layer antimonene.¹²⁵

With this knowledge in mind, it is apparent that the surface oxidation of antimonene is in most cases inevitable, especially if exposed to ambient conditions. It becomes vital, now more than ever before, to reconsider the outcomes of such drastic surface changes on the measured physical properties of antimonene, which might eventually lead to the better understanding of the current divergence in the reported experimental findings. Furthermore, it might also explain the difficulties being encountered by different research groups in conducting some of what is considered basic measurements in the realm of 2D materials, such as electrical contacts and determination of the electronic band gap.

Through this section of the present review, we aim at stimulating the scientific community to revive the discussions related to this fundamental aspect of antimonene. For instance, Gibaja *et al.* observed that the ultrasonication-induced oxidation of liquid-phase exfoliated antimonene comparatively enhanced the electrocatalytic performance towards the hydrogen evolution reaction (HER) under acidic pH.¹¹² Likewise, Bat-Erdene *et al.* demonstrated that surface-oxidized few-layer antimonene nanosheets can be an efficient nitrogen reduction reaction (NRR) catalyst for the electrochemical synthesis of NH_3 .¹⁶⁹ According to the same authors, the activation of the NN bond for the NRR process is facilitated by the oxidized species of antimonene as a result of the more favourable adsorption energy of N_2 caused by the increase in polarity, as compared to non-oxidized antimonene. Furthermore, Duo *et al.* proved that ultrathin antimonene nanoparticles (AMNPs) are effective radiosensitizers that can achieve efficient radiochemotherapeutic effects.¹⁷⁰ As the authors explained, X-ray irradiation induced reactive oxygen species (ROS) overproduction and accelerated the valence transition to toxic Sb_2O_3 , eventually leading to cancer cell death. Finally, yet importantly, it turned out that the oxidation of antimonene is highly desired in many applications, as opposed to the detrimental oxidation of black phosphorus. Therefore, the development of a fast, effective, and reliable method to realize the expected antimonene oxide

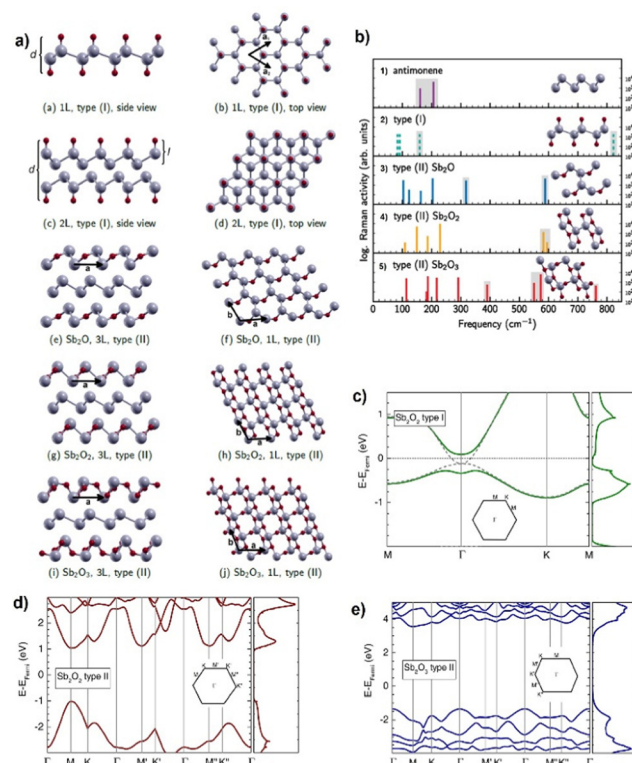


Fig. 23 (a) Type (I) antimonene oxide structures with one layer in side view (a) and top view (b), and two layers in (c) and (d). Type (II) antimonene oxide heterostructures with different stoichiometries of the oxidized layers: (e) and (f) Sb_2O ; (g) and (h) Sb_2O_2 ; and (i) and (j) Sb_2O_3 . Type (III) structures in the top view show the oxidized layer only. Oxygen (antimony) atoms are shown in red (gray). Labels a and b on the figures indicate the in-plane lattice vectors. (b) Calculated frequencies of Raman-active vibrational modes in (1) antimonene, (2) type (I), (3)–(5) type (II) antimonene oxide structures. (c)–(e) Electronic band structures and density of states calculated using the hybrid functional HSE12 and inclusion of spin–orbit interactions (SOI) for (c) type (I) Sb_2O , (d) type (II) Sb_2O_2 , and (e) type (II) Sb_2O_3 monolayers. Gray dashed lines are the results without SOI and are almost congruent with the bands with SOI for (c) and (d). The zero of energy is set to the Fermi energy. Adapted from ref. 168 with permission from American Physical Society, copyright 2022.

systems is an urgent demand. Fickert *et al.* have recently introduced a proof of concept of such a method, by which they realized arbitrary heterostructures of Sb_2O_3 /antimonene through a spatially resolved laser-induced oxidation of antimonene on the sub- μm scale.⁹⁸ Although a fine control of the O distribution and concentration is still to be achieved, it provides an indisputable experimental evidence of its practical feasibility. In the same context, Han *et al.* have successfully synthesized two-dimensional Sb_2O_3 crystals down to the monolayer thickness using passivator-assisted vapour deposition (PAVD) (Fig. 24).¹⁷¹ The crystal structure and chemical composition have been confirmed by a set of analytical techniques, namely SAED, HAADF-STEM, EDX and EELS (Fig. 24(d)–(f) and (i)–(l)). Interestingly, the authors unravelled a reversible phase transition between α - and β -phases of Sb_2O_3 , which could be controlled either by thermal annealing or by electron-beam irradiation. This remarkable phase transformation is accompanied



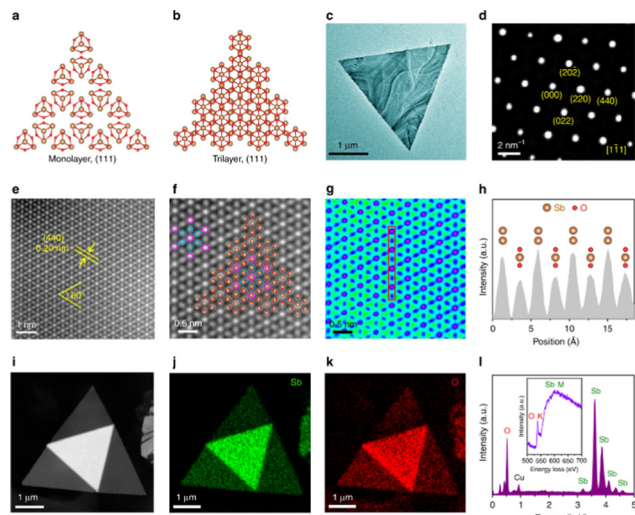


Fig. 24 Atomic structure of 2D Sb_2O_3 molecular crystals. (a), (b) Top-view structural models of monolayer and trilayer Sb_2O_3 flakes with the (111) plane. Brown balls, Sb atoms. Red balls, O atoms. (c) TEM image of a triangular Sb_2O_3 flake. (d) SAED pattern of the Sb_2O_3 flake. (e) Z-contrast atomic-level HAADF-STEM image of the Sb_2O_3 flake showing the perfect atomic lattice. (f) Enlarged HAADF image and the matched atomic ball model, white atoms are marked by yellow circles and gray atoms are marked by blue circles. (g) Scattered electron intensity color image for (f). (h) Intensity line profile along the red box in (g). (i)–(k) HAADF image of a stacked flake and the corresponding elemental maps for Sb and O. (l) EDX and EELS spectra of the Sb_2O_3 flake. Reproduced from ref. 171 with permission from Springer Nature, copyright 2019.

by changes in the electrical properties of the crystals which switches from the insulating α -phase of Sb_2O_3 to the semiconducting β -phase, thus demonstrating their potential applications in phase-change devices.

Last but not least, in contrast to predicted good semiconducting behaviour, experimental reports on antimonene have proved semimetal to semiconductor transitions, high carrier mobilities and strain-tunable indirect-to-direct bandgap transition, as well as the possibility of 2D and 3D topological insulator behaviour. However, due to the large allotropic/polymorphic structural diversity of antimonene, the preparation of structurally controlled ultrathin high-quality samples is very challenging. Indeed, from the physical point of view, the preparation of laterally large, defect-free monolayer antimonene films is the most important synthetic challenge. It is due to the lack of free-standing high-quality monolayer samples for device fabrication that some open questions regarding transport properties of antimonene remain unexplored. We believe that future synthetic efforts should pursue to tackle this challenge. Furthermore, once this hurdle has been overcome, the interesting topologically surface state physics of antimonene will allow its application in quantum computing or spintronic devices to be envisioned.

4.2 Chemical functionalization

Contrary to other 2D materials such as graphene or even other pnictogens like phosphorene,^{60,118,172} the chemical functionalization of antimonene is barely explored. Very scarce reports can be found in the literature regarding this topic.

After initial predictions concerning the effect of adatoms and physisorbed molecules on the overall properties of antimonene,^{96,173} the first experimental evidence of a noncovalent functionalization was reported by Abellán *et al.* in 2017.¹⁶⁶ In that work, the authors report the functionalization of antimonene with perylene diimide (PDI), resulting in a higher charge-transfer performance than that observed in black phosphorus (Fig. 25). The functionalization was carried out by drop-casting a THF solution of a tailormade

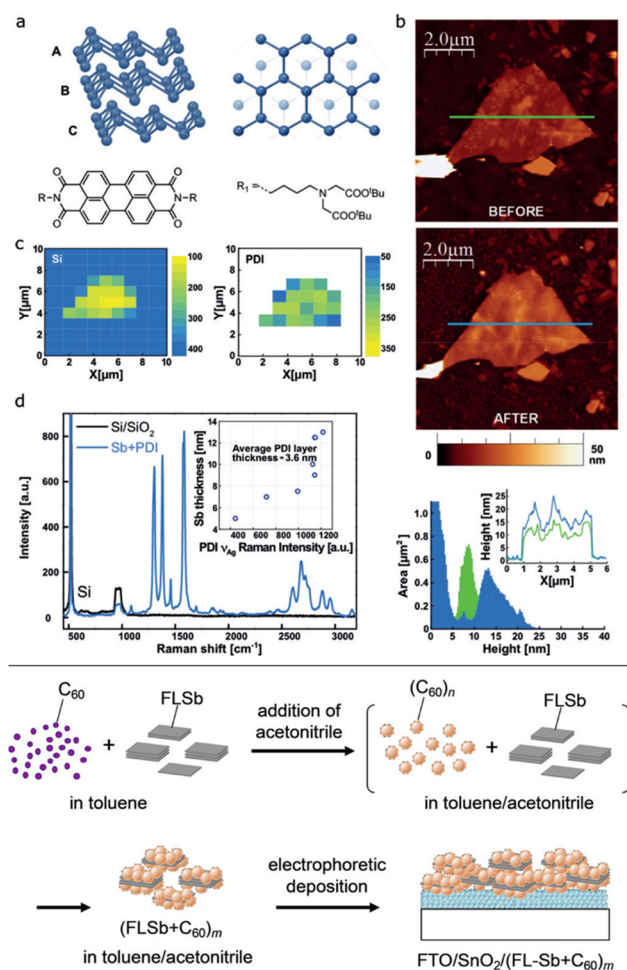
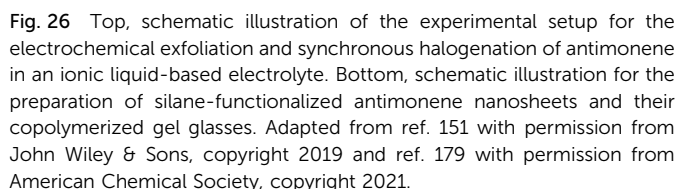


Fig. 25 Top: (a) Structure of β -antimonene (top panel) and the perylene bisimide (PDI) molecule (bottom panel). (b) AFM topographic images showing an antimonene flake of about 10 nm of thickness. Top: Flake as deposited. Middle: Same flake after the functionalization with PDI molecules. Bottom: Height histograms of the flake before (green) and after functionalization (blue), showing an average thickness increase of 4.1 nm. The average PDI coverage in all the studied flakes was 3.6 nm. The inset shows representative profiles corresponding to the lines in the images. (c) Scanning Raman microscopy (SRM) of the same flake. Left: Silicon intensity Raman map showing a decrease in the 521 cm^{-1} signal which clearly reveals the morphology of the flake. Right: Raman intensity mapping shows the exclusive self-assembly of the PDI on the antimonene flakes and not on the Si/SiO_2 substrate. (d) Mean Raman spectra (excitation at 532 nm) of the flake showing the PDI bands as a consequence of the quenching of its fluorescence. Bottom: Formation and electrophoretic depositions of FLSb- C_{60} composite clusters. Adapted from ref. 166 and 176 with permission from John Wiley & Sons, copyright 2017 and 2020.



In addition to the noncovalent functionalization previously reported with discrete molecules, Zamora and co-workers

Finally, the covalent functionalization of antimonene has been recently reported by Xing *et al.* using 3-glycidioxypropyltrimethoxysilane achieving silane-functionalization.¹⁷⁹ Silane



Rao *et al.* also covalently functionalized antimonene and bismuthine nanosheets using *p*-nitrobenzene diazonium salts.¹⁸³ The study of the reaction mechanisms demonstrated the transfer of lone pairs of electrons from the metallic Sb to

As previously commented in this review, the practical applications and properties of antimonene are still emerging. However, there are different works that propose a broad range of feasible applications, including proof-of-concept devices and processes that can be classified into optoelectronic devices, catalysis and electrocatalysis, energy storage, and last but not least, in biomedical applications like cancer therapy or biosensing, which we believe holds great promise for the following years. Below we will detail each of them, showing their potential and future prospects.

Optoelectronic devices require materials that are both responsive to visible light as well as able to transfer carriers. In this sense, 2D conductors benefit from appropriate bandgaps and high mobilities.^{15,184} From the practical point of view, Wang *et al.* reported the first use of antimonene with the adequate bandgap as a hole transport layer (HTL) in a perovskite solar cell (Fig. 27).¹⁸⁵ The assembled device was built as an ITO/antimonene/perovskite/PCBM/Bphen/Al heterostructure (PCBM = [6,6]-phenyl-C61-butyric acid methyl ester). Antimonene was obtained after pregrinding bulk Sb into Sb plates that were transformed into antimonene by means of LPE assisted by sonication. The final material was obtained after successive centrifugation at different speeds while studying the bandgap dependence on the thickness, which was tuned in the 0.8 to 1.44 eV range (probably related with different degrees of surface oxidation). The energy level of antimonene closely matches that of methylammonium lead iodide (MAPbI₃) perovskite, hence suggesting an adequate driving force for the hole extraction. This fact is also confirmed by the strongly quenched photoluminescence of the perovskite on top of the ITO/antimonene. This is indicative of the prevented radiative recombination due to photoinduced charge separation. The use of the material as an HTL gave rise to an enhancement of in the hole extraction and photocurrent of *ca.* 30%, from 11.2 to 14.6 mA cm⁻² for the HTL-free (control sample) and the antimonene device, respectively. In addition, the external quantum efficiency (EQE) in the entirely visible light was enhanced from 45% to 55–60% for the control and antimonene device, respectively. Additionally, Wang *et al.* also reported the use of antimonene quantum dots (AMQDs) for assembling high-performance organic photovoltaics, enhancing the power conversion efficiency of the device *ca.* 25% higher than that compared with the reference device (Fig. 27).¹⁸⁶

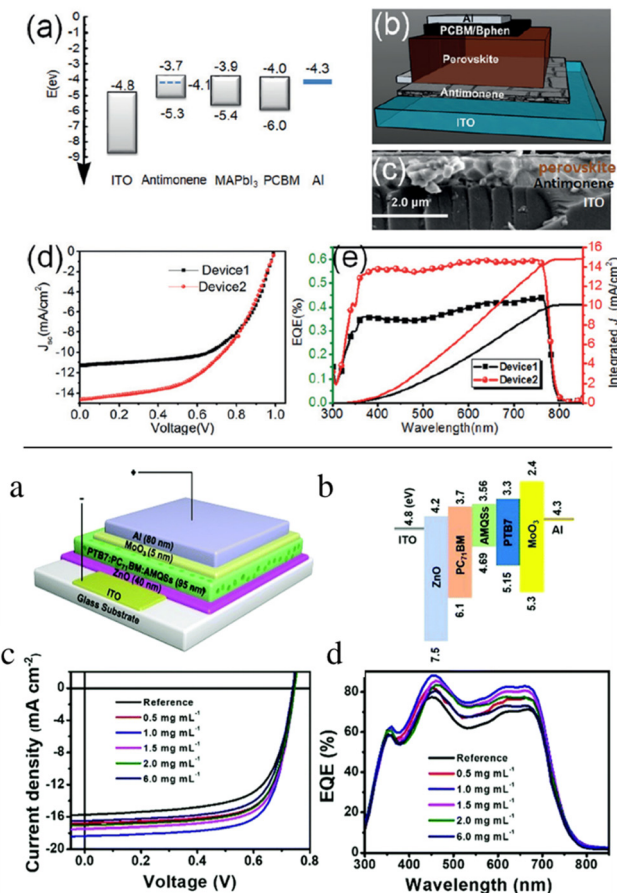


Fig. 27 Top: (a) Comparison of energy levels of each functional layer. The Fermi level of antimonene is represented by the dashed line. (b) Configuration of the antimonene-based device. (c) Cross-sectional SEM image of the studied device. (d) Current-density-voltage (J - V) curves of devices with different architectures. (e) External quantum efficiency (EQE) spectra together with EQE-data-based integrated short-circuit current densities (J_{sc}) for devices 1 (HTL-free) and 2 (ITO/antimonene/perovskite/PCBM/Bphen/Al). Bottom: Device structure and performance characterization of an antimonene organic-photovoltaics device. (a) Device architecture including the AMQDs. (b) Band structure of the organic-photovoltaics device. (c) Current density-voltage (J - V) curves and (d) EQE characteristics of the best reference device and the devices with different concentrations of AMQDs in their active layer. Adapted from ref. 185 with permission from John Wiley & Sons, copyright 2018, and ref. 186 with permission from the Royal Society of Chemistry, copyright 2018.

After the work of Wang *et al.*,¹⁸⁵ other authors have proposed additional works on the optoelectronic applications. Lu *et al.* reported α -phase few-layer antimonene and AMQDs with nonlinear optical Kerr response using spatial self-phase modulation (SSPM).¹²⁶ They reported a nonlinear refractive index of the few-layer antimonene of *ca.* 10^{-5} cm² W⁻¹, larger than that of AMQDs. Therefore, the study proposes antimonene as a new kind of promising optical Kerr material with enhanced stability, particularly at a short wavelength range. Song *et al.* also reported the study of the broadband nonlinear optical response of few-layer antimonene *via* open-aperture Z-scan laser measurement.¹⁸⁷ Their findings confirmed the use of a few-layer antimonene decorated microfiber as an optical

saturable absorber for ultrafast photonics operation and as a stable all-optical pulse thresholder that can suppress the transmission noise, boost the signal-to-noise ratio (SNR), and reshape the deteriorated input signal.¹⁸⁷ That work was further expanded with an additional study in which they use the microfiber as an all-optical Kerr switcher with an extinction ratio up to 12 dB and a wavelength conversion of modulated high-speed signals at a frequency up to 18 GHz.¹⁸⁸ Both reports enlighten the applicability of antimonene-based devices in high-speed optical communication. Finally, the work of Zhang *et al.* demonstrated that semiconducting antimonene nanosheets (probably heavily oxidized ones) exhibited indirect bandgap properties with photoluminescence bandgap of *ca.* 2.33 eV and a lifetime of 4.3 ns. These nanosheets were also satisfactorily tested for the hole extraction layer in planar inverted perovskite solar cells, enhancing the device performance thanks to fast hole extraction and efficient hole transfer at the perovskite/hole transport layer interface.¹⁸⁹

Alongside optoelectronic applications, the preparation of electronic devices as field effect transistors (FETs) is also reported with antimonene. In this topic, Ji *et al.* reported the fabrication of thin film transistors on few-layer antimonene.¹¹⁷ The devices were directly prepared on mica substrates after the synthesis of β -antimonene using HfO₂ as a top gate dielectric. The contacts are made of Cr and Au in the form of 10 and 30 nm thick layers, respectively. Afterwards, a 15 nm thick layer of HfO₂ was grown on the top by means of atomic layer deposition, followed by a final 50 nm thick layer of Au as the top gate electrode. The electrical characterization was carried out with a semiconductor parameter analyser at room temperature, and three typical devices with antimonene thicknesses of 30, 40 and 50 nm were measured at zero gate bias. Regarding the thinnest device (30 nm), an electrical resistance of 600 Ω was measured, with an electrical conductivity of 1.6×10^4 S m⁻¹. This value is in good agreement with that expected for semimetals and consistent with the theoretical predictions. Furthermore, the antimonene devices on mica substrates exhibited high flexibility and no major changes in the conductivity were observed after bending 100 times. These results combined with the wavelength independent high transparency in the visible light range suggest antimonene as a good candidate in the elaboration of flexible transparent conducting electrodes.¹¹⁷

Further studies on preparing transistors are found in the works of Chang¹⁹⁰ and Sun *et al.*¹⁹¹ The first one is focused on novel antimonene tunneling field-effect transistors (TFETs) based on the lateral monolayer (semiconducting)/multilayer (metallic)/monolayer (semiconducting) heterostructure. The proposed antimonene TFETs consist of a semiconducting monolayer of the material in combination with a small metallic multilayer region between the source and the channel. The presence of a multilayer region introduces gapless metallic states that result in the enhancement of the tunneling probability, leading to a larger current. Using the *ab initio* electronic structure and quantum transport calculations for different antimonene TFETs, the simulations conclude that even a



5.2 Electrocatalysis

Most recently, Gibaja *et al.* reported the electrocatalytic properties of LPE-antimonene suspended in BuOH or NMP towards the hydrogen evolution reaction (HER).¹¹² In this study, two parameters were chosen to compare the electrochemical performance: the Tafel slope and the overpotential required at a current density of 10 mA cm⁻² (Fig. 28). The antimonene prepared in NMP showed a lower Tafel slope (145 mV dec⁻¹) than the antimonene prepared in BuOH, while the latter depicted a lower overpotential value (-0.7 V). The reduction in the onset potential could be ascribed to both the dimensions of the nanosheets and the oxidation degree. Cyclic voltammetry curves before and after the linear sweep voltammetry showed a more pronounced redox activity for the sample in BuOH. These results are indicative of a higher degree of exfoliation of the sample in BuOH than that prepared in NMP. The cyclic voltammetry curves also highlight the irreversible oxidation processes which indicate the oxidation of antimonene into novel surface Sb oxides with specific structural and physical properties. Overall, the higher HER performance of the BuOH sample can be explained based on its better exfoliation degree and anisotropic ratio, which yield a large number of edges and therefore electroactive sites. This HER performance is also linked to the irreversible formation of Sb oxides, an effect which is more pronounced in the BuOH sample than in the NMP one.¹¹²

Lewis acid catalysis is a chemical process that is mainly based on the ability of protons and/or cationic metal atoms to attract electron density from atoms of external molecules and activate them towards the attack of a third chemical entity. However, the use of non-metal species, beyond protons, is much scarcer, in particular of heteroatoms in the low-valence state. Pnictogens in the zero oxidation state (P, As, Sb, Bi) are rarely used in catalysis because of the difficulties in preparing stable materials from these elements. Nonetheless, Lloret *et al.* recently reported the first organic catalysis for antimonene and phosphorene taking advantage of the high degree of exfoliation and the protection against oxidation given by the ionic liquid used in the LPE process. The work focuses on the use of few-layered pnictogens as efficient catalysts for the alkylation of nucleophiles (alcohols, thiols and indoles) with alkyl carbonyl compounds (esters) in good yields and excellent selectivity (Fig. 29).⁶⁵ Regarding the reaction mechanism, it is observed that the pnictogen selectively adsorbs both the nucleophile and

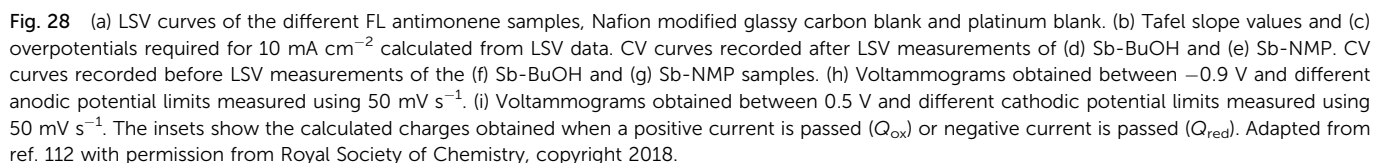
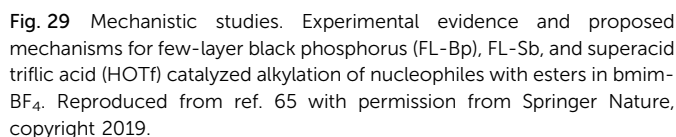


Fig. 28 (a) LSV curves of the different FL antimonene samples, Nafion modified glassy carbon blank and platinum blank. (b) Tafel slope values and (c) overpotentials required for 10 mA cm⁻² calculated from LSV data. CV curves recorded after LSV measurements of (d) Sb-BuOH and (e) Sb-NMP. CV curves recorded before LSV measurements of the (f) Sb-BuOH and (g) Sb-NMP samples. (h) Voltammograms obtained between -0.9 V and different anodic potential limits measured using 50 mV s⁻¹. (i) Voltammograms obtained between 0.5 V and different cathodic potential limits measured using 50 mV s⁻¹. The insets show the calculated charges obtained when a positive current is passed (Q_{ox}) or negative current is passed (Q_{red}). Adapted from ref. 112 with permission from Royal Society of Chemistry, copyright 2018.



The higher polarizability of the antimonene results in a better performance than that found for the phosphorene. This mechanism enables Lewis acid catalysed processes under much milder conditions than with protons or metal cations, giving access to the alkylation of soft nucleophiles incompatible with the standard acid catalyzed conditions. This result is also in good agreement with the ability of antimonene to transfer electron charge to planar aromatic molecules, as shown in the noncovalent functionalization studies previously analyzed.¹⁶⁶

The use of antimonene in energy storage is focused on its application as an anode in Na storage thanks to its high theoretical capacity of 660 mA h g^{-1} for Na storage as well as a low discharge potential of *ca.* 0.5 V (*versus* Na^+/Na).¹⁹⁸ It is worth noting that Na-ion batteries (SIBs) have attracted increasing attention because of sodium abundance, affordability, ease and greenness of extraction procedure.¹⁹⁹ Nonetheless, the larger size of Na^+ compared to Li^+ , the slow insertion and extraction of ions, and large volume changes represent the main drawbacks for developing sodium-ion batteries (NaIBs). In this sense, 2D materials in general, and 2D-pnictogens in particular, are considered one of the best alternatives for electrode materials.

In fact, Gu *et al.* reported the synthesis of composite films made of antimonene nanosheets and graphene.¹²⁴ The synthesis of Sb nanosheets was carried out *via* LPE starting from Sb powder in an IPA solution with constant concentration of NaOH. The resulting composite films were prepared with

measured at a current density of 14 A g^{-1} , hence being considered as a highly promising material for energy storage applications. In line with that, the system also exhibited a highly competitive energy and power densities of 20 mW h kg^{-1} and 4.8 kW kg^{-1} , respectively, in combination with good cycling capabilities. It is worth mentioning that the optimum capacitive performance has been achieved for quantities of 3.6 ng of antimonene/SPE.

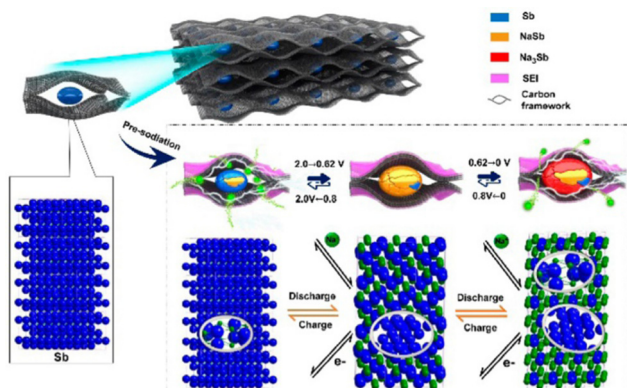
5.5 Biomedical applications

5.5.1 Cancer therapy. Among the different techniques related to cancer therapy, photothermal therapy (PTT) is considered as one of the most promising strategies thanks to its high efficiency and minimal invasiveness.²⁰² Therefore, it is necessary to develop photothermal agents (PTAs) with both good biocompatibility and excellent photothermal conversion efficacies (PTCEs).

Finally, Zamora and co-workers have recently reported the use of antimonene in modified screen-printed electrodes (SPE) for supercapacitors.²⁰¹ They reported a significant improvement in the energy storage capabilities of a carbon electrode in both galvanostatic charging and cyclic voltammetry using 0.5 M H₂SO₄ as the electrolyte. Antimonene depicted an excellent performance with a specific capacitance of 1578 F g⁻¹

In this sense, Tao *et al.* reported the synthesis of novel PTAs using AMQDs coated with PEG *via* LPE.¹²⁷ The surface modification of AMQDs with PEG enhanced the biocompatibility and stability in the physiological medium (Fig. 31). The authors reported a clear dependence of the photothermal effect with the concentration, showing a PTCE of 45.5%, higher than that observed for other PTAs such as graphene, MoS₂ or black phosphorus.²⁰³ By measuring the *in vitro* cytotoxicity of the PEG-coated AMQDs all samples exhibited good biocompatibility. Nevertheless, it was observed that the cellular viability decreased when the AMQD concentration increased under near-infrared (NIR) radiation. This decrease was reported to be down to 10% of viable cells at a 200 $\mu\text{g mL}^{-1}$ concentration. Fig. 31 depicts a clear separation between the living and dead cells, coloured in green and red, respectively, thus confirming the killing of cancer cells using AMQDs as a PTA combined with NIR radiation. Additionally, *in vivo* studies were carried out in mice with MCF-7 tumours, confirming the successful treatment of NIR irradiation combined with intratumour injection of PEG-coated AMQDs, resulting in negligible or no regrowth of the tumour. In this line, Niu *et al.* also focused on the PTCEs of AMQDs presenting the first excited-state dynamics study of the PTT of antimonene. Interestingly, this work highlights that the enhanced PTT of AMQDs comes from their spontaneous partial oxidation. This feature induces additional band edge states that broaden the optical absorption range and strengthen the transition dipole moment. Henceforth, this study proposes the use of oxidative AMQDs in the biomedical field.²⁰⁴

Most recently, the same authors reported a photonic drug-delivery platform based on 2D PEGylated antimonene nanosheets.²⁰⁵ The main advantages of this platform are its excellent photothermal properties, high drug-loading capacity, spatiotemporally controlled drug release activated by NIR light and moderate acidic pH, deep tumour penetration by both extrinsic and intrinsic stimuli, excellent multimodal-imaging properties or substantial inhibition of tumour growth with no



This journal is © The Royal Society of Chemistry 2023

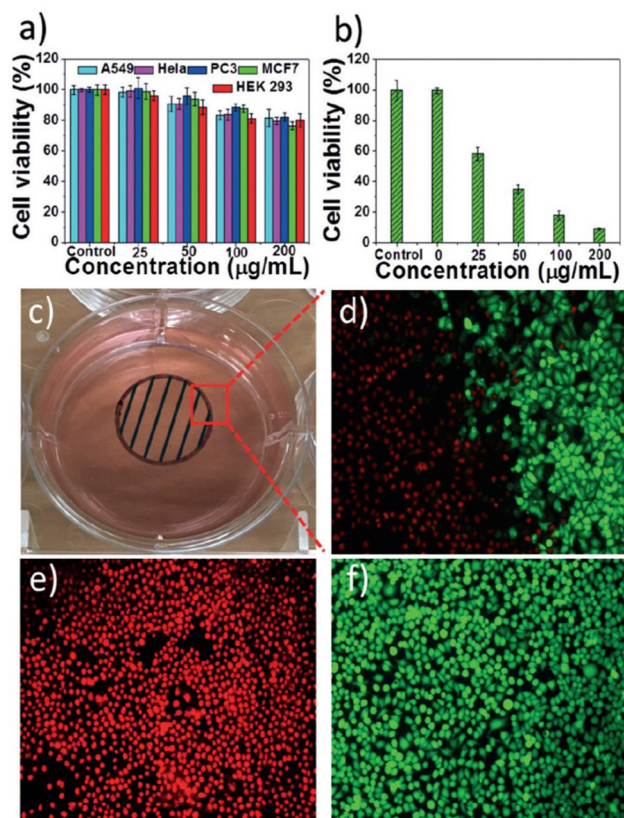


Fig. 31 (a) Cell viability after incubation with only PEG-coated AMQDs. (b) Cell viability of MCF-7 cells treated with PEG-coated AMQDs with NIR (808 nm, 1 W cm^{-2}) for 5 minutes. (c) A photo of the cell culture dish after incubation with PEG-coated AMQDs. The black circle with shadow shows the laser spot. (d)–(f) Confocal images of calcein antimonene (green, live cells) and propidium iodide (PI) (red, dead cells) co-stained MCF-7 cells after exposure to NIR irradiation (808 nm, 1 W cm^{-2}). The amplification of confocal images is $100\times$. Reproduced from ref. 127 with permission from John Wiley & Sons, copyright 2017.

apparent side effects and potential degradability, to name a few. Furthermore, the intracellular fate of the antimonene nanosheets was revealed for the first time, leading to a better understanding of the nano-bio interactions of this class of 2D materials. The work of Tao *et al.* represents the first study on antimonene-based photonic drug-delivery platforms, hence paving the way for the application of this pnictogen into cancer theranostics (Fig. 32).²⁰⁵

Additionally, Lu *et al.* also reported the successful use of antimonene for high-performance cancer theranostics.²⁰⁶ In this case, the authors propose the use of cell membrane camouflage alongside dimension optimization and size control to improve the stability of antimonene. The need for enhancing the stability of this material is crucial since its use as a photothermal therapy agent is limited by its rapid degradation in physiological medium. Therefore, the antimonene sheets cloaked with the cell membrane exhibited improved stability as well as increased photothermal efficacy and superior tumour targeting capacity. Furthermore, no notable side effects were observed after using the coated antimonene as a potent

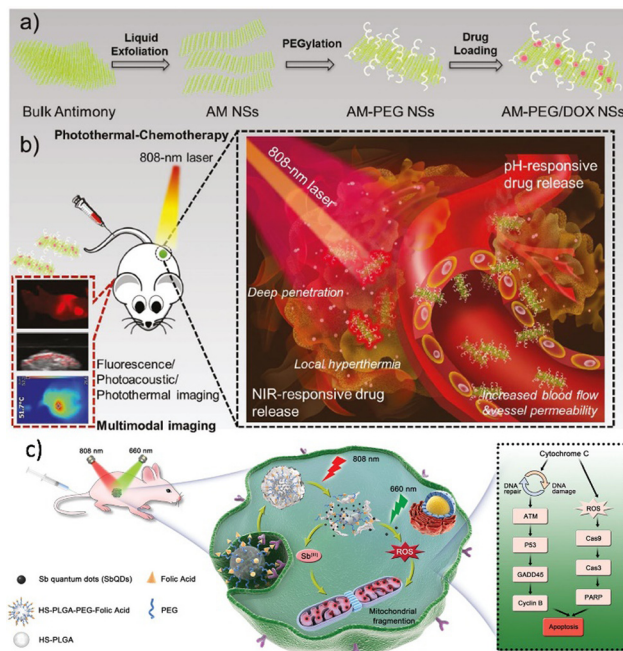


Fig. 32 Schematic illustration of (a) the preparation of 2D antimonene-PEG-doxorubicin nanosheets and (b) their administration as photonic nanomedicines for cancer theranostics, (c) Nanopoxia treatment and methods of action. Adapted from ref. 205 and 206 with permission from John Wiley & Sons, copyright 2018 and 2020.

photodynamic/photothermal therapy agent as an anticancer treatment during *in vivo* studies. In conclusion, this strategy reveals as a safe and high-performance modality of cancer therapy.²⁰⁷

One of the current challenges that photothermal therapy faces is the activation of inherent defence mechanisms of tumorous cells due to the overexpression of heat shock proteins in response to the hyperthermia-based treatments. To prevent this thermoresistance, Wu *et al.* constructed a nanocatalyst consisting of calcium carbonate, glucose oxidase and AMQDs.²⁰⁸ When the nanocatalyst encounters the acidic tumour microenvironment, it rapidly degrades releasing the integrated glucose oxidase and the AMQDs. The enzymatic activity of glucose oxidase effectively depletes the cellular glucose levels, reducing energy supplies of the tumorous cells and down-regulating the expression of the heat shock proteins, increasing the therapeutic performance of the photonic hyperthermia treatment. This study reveals the potential of multimodal synergistic therapies for improved biomedical effects.

Interestingly, Qiu *et al.* recently presented a proof-of-concept of an hypoxia-based precision cancer therapy, which they called nanopoxia.²⁰⁹ Taking advantage of the hypoxia conditions usually found in tumours, they developed a nanoplatform based on AMQDs encapsulated by a thermosensible polymer. Upon 808 nm laser irradiation, the SbQDs@HS-PLGA-PEG-FA outer shell is degraded, releasing the antimonene nanoparticles. In the hypoxic environment of tumours, Sb is



Finally, Song *et al.* investigated an effective strategy to synthesize Sb nanocrystals in ligand-guided growth strategy, observing a modulation effect on the localized surface plasmon resonance depending on the morphology on the obtained antimony nanopolyhedra.²¹⁰ This allowed them to increase the PTCE up to 62% when the excitation wavelength is well matched with the resonance frequency of the particles. This finding demonstrates the importance of morphology-controllable synthesis methods, allowing the fine tuning of the properties of the Sb-nanomaterials for maximizing their therapeutic potential. These results may serve as inspiration for future developments in antimonene chemistry.

5.5.2 Biosensing. Biosensing applications have been reported for elemental 2D materials such as graphene or phosphorene, taking advantage of the large surface area and the possibility of stabilizing different (macro)molecules by supramolecular interactions.^{211,212} Similarly, the first report showing the use of antimonene as a biosensor was reported by Mayorga-Martínez *et al.*²¹³ In that work, the authors optimized and implemented a highly sensitive and selective phenol enzymatic biosensor using exfoliated antimonene (among other pnictogens) as the sensing platform to enhance the electron transfer process. The resulting biosensor was used for phenol detection following the electroreduction of o-quinone to catechol (Fig. 33). The pnictogen nanosheets were obtained by shear-force exfoliation that underwent a downsizing process alongside the delamination of the material. The phenol biosensor based on antimonene exhibited the best results among the tested pnictogens (phosphorene, arsenene, antimonene and bismuthene), with enhanced analytical performance from the point of view of sensitivity, selectivity, linearity and reproducibility. Furthermore, the boosted electrocatalytic reduction of phenol allows its detection in the presence of common interferents and real samples, with LOQ and LOD 10 times below the recommended limit.²¹³

Another study in the field of sensing can be found in the work of Xue *et al.*²¹⁴ reporting a surface plasmon resonance sensor which is based on 2D antimonene, with the aim of the label-free detection of clinically relevant bio-markers such as miRNA-21 and miRNA-155. By means of first-principles

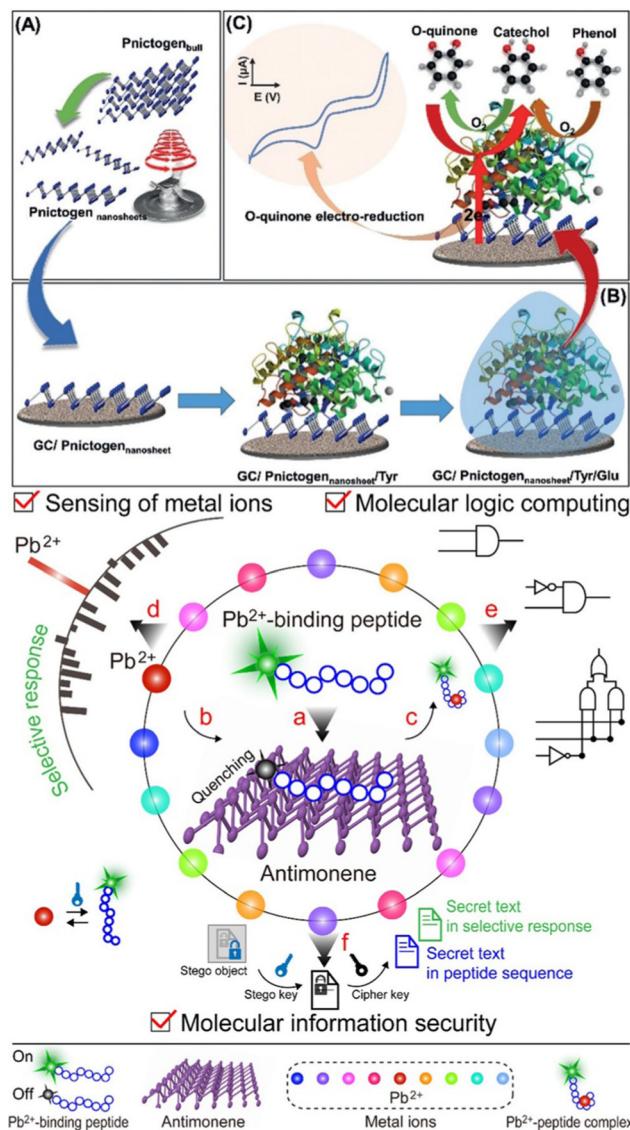


Fig. 33 Top (a) Shear exfoliated pnictogens using a kitchen blender. (b) Biosensor preparation using layer-by-layer drop-cast pnictogen nanosheets, tyrosinase (Tyr), and glutaraldehyde (Glu) onto a glassy carbon (GC) electrode. (c) Chemical mechanism of phenol detection by a biosensor based on exfoliated pnictogen and Tyr. Bottom, scheme of a peptide fluorescence sensing system using antimonene and its different applications in the detection of Pb^{2+} , molecular logic operations and crypto-steganography. Adapted from ref. 212 with permission from John Wiley & Sons, copyright 2019, and ref. 217 with permission from American Chemical Society, copyright 2022.

energetic calculations it is estimated that antimonene exhibits stronger interaction with single-stranded DNA than graphene because of the more delocalized 5s/5p orbitals in antimonene. With an enhanced LOD up to 10,000 times compared to existing miRNA sensors, antimonene reveals as a promising material in the development of these biosensors.²¹⁴

Taking advantage of this surface plasmon resonance, Singh *et al.* developed a nanolayered biosensing device for the detection of hemoglobin concentrations, by combining BaTiO₃ and antimonene.²¹⁵ In this device the antimonene is used as the

As previously discussed, antimonene shows a great potential in the biomedical field, with the first studies reporting the use of this material as PTA showing its great PTCE, together with an excellent biocompatibility of the PEG coated antimonene, both *in vitro* and *in vivo*.^{127,205,206} In terms of toxicity, the coated

Getting the picture of what happens with antimonene when it interacts with the biological environments (cell culture media and/or blood plasma) up to the subcellular fate of the material, addressing the alterations that it may suffer, is not an easy task. From the moment that antimonene enters in contact with the cell culture media, protein–nanoparticle interactions form the protein corona, which might affect the antimonene chemical stability and undoubtedly affects the cellular response towards the nanomaterial.^{220,221} The surface modification plays a crucial role in its uptake and internalization, as it is intimately related to the size, shape and surface chemistry of the nanoparticles, affecting the relative contribution of the uptake route.^{218,219} This in turn affects the intracellular fate of antimonene, as each internalization mechanism has different trafficking pathways, ending in diverse subcellular compartments. It is important to keep in mind that cellular organelles and compartments have utterly different chemical environments, from neutral pH compartments like endosomes or caveosomes, high molecular density organelles as the nucleus, or even very acidic and very enzymatic active lysosomes, which could affect the chemical evolution of the nanomaterial, probably modifying the nanomaterial toxicity and response. The reliable assessment of the nanomaterial and cellular association appears as a key factor in understanding the role of novel nanomaterials as biomedical tools. Nevertheless, there is no single analytical methodology capable of providing all the required information, compelling a multimodal approach, a promising strategy that offers analytical and statistical evidence to be able to obtain the full picture of these complex processes.²²³

This review summarizes the most important aspects of anti-monene highlighting why it is considered as one of the most promising 2D materials for energy storage, high-performance opto-electronic devices, DNA sensors, cancer therapy or novel vdW heterostructures, to name a few. From its properties to its

In terms of applications, the use of different forms of antimonene in optoelectronic devices holds great promise in field effect transistors, perovskite solar cells or non-linear optics. It is worth mentioning that in some cases the oxidized $\text{Sb}_x\text{O}_y/\text{Sb}$ heterostructures outperform pristine antimonene, emphasizing the importance of controlling the synthesis of the materials. Particularly, this aspect represents one of the main differences with lighter 2D-pnictogens as phosphorene, in which surface oxidation leads to a complete degradation of the flakes. The surface reactivity of antimonene has turned out to be key for the development of catalysts, both for boosting organic reactions or electrochemical processes. In fact, while in

Last but not least, access to monodisperse systems such as AMQDs or colloidal routes open the door to one of the most suggestive fields of application of antimonene: biomedicine. In this direction, to the best of our knowledge, there is a lack of systematic studies aiming to rationalize the chemical identity of bare antimonene (synthetic method, size, morphology and surface chemistry) on the biomedical performance of the material, hampering the comprehension of the mechanisms governing the cellular response towards antimonene and *vice versa*. It will be paramount to understand the mechanism controlling the uptake of antimonene nanomaterials and how they are influenced by its physicochemical properties, as well as depicting the toxic mechanism of antimonene, relating them to the chemical evolution that it may suffer during the interaction (*e.g.* oxidation). A methodical study of how the properties of antimonene affect its biological performance will allow a rational design of novel antimonene biomedical platforms, with control over their stability, toxicity and biodistribution, enabling more precise biomedical nanodevices based on this novel nanomaterial. Overall, we hope that this review article will inspire novel research regarding antimonene paving the way for the development of new exciting applications.

There are no conflicts to declare.

This work has been supported by the European Union (ERC-2018-StG 804110-2D-PnictoChem to G. A.), the Spanish MICINN (PID2019-111742GA-I00, PDC2022-133997-I00, TED2021-131347B-I00 and Excellence Unit María de Maeztu CEX2019-000919-M),

References

- 1 G. Fiori, F. Bonaccorso, G. Iannaccone, T. Palacios, D. Neumaier, A. Seabaugh, S. K. Banerjee and L. Colombo, Electronics Based on Two-Dimensional Materials, *Nat. Nanotechnol.*, 2014, 9(10), 768–779, DOI: [10.1038/nnano.2014.207](#).
- 2 Y. Zhang, A. Rubio and G. L. Lay, Emergent Elemental Two-Dimensional Materials beyond Graphene, *J. Phys. D: Appl. Phys.*, 2017, 50(5), 053004, DOI: [10.1088/1361-6463/aa4e8b](#).
- 3 N. R. Glavin, R. Rao, V. Varshney, E. Bianco, A. Apte, A. Roy, E. Ringe and P. M. Ajayan, Emerging Applications of Elemental 2D Materials, *Adv. Mater.*, 2020, 32(7), 1904302, DOI: [10.1002/adma.201904302](#).
- 4 S. Z. Butler, S. M. Hollen, L. Cao, Y. Cui, J. A. Gupta, H. R. Gutiérrez, T. F. Heinz, S. S. Hong, J. Huang, A. F. Ismach, E. Johnston-Halperin, M. Kuno, V. V. Plashnitsa, R. D. Robinson, R. S. Ruoff, S. Salahuddin, J. Shan, L. Shi, M. G. Spencer, M. Terrones, W. Windl and J. E. Goldberger, Progress, Challenges, and Opportunities in Two-Dimensional Materials Beyond Graphene, *ACS Nano*, 2013, 7(4), 2898–2926, DOI: [10.1021/nn400280c](#).
- 5 D. Geng and H. Y. Yang, Recent Advances in Growth of Novel 2D Materials: Beyond Graphene and Transition Metal Dichalcogenides, *Adv. Mater.*, 2018, 30(45), 1800865, DOI: [10.1002/adma.201800865](#).
- 6 G. R. Bhimanapati, Z. Lin, V. Meunier, Y. Jung, J. Cha, S. Das, D. Xiao, Y. Son, M. S. Strano, V. R. Cooper, L. Liang, S. G. Louie, E. Ringe, W. Zhou, S. S. Kim, R. R. Naik, B. G. Sumpter, H. Terrones, F. Xia, Y. Wang, J. Zhu, D. Akinwande, N. Alem, J. A. Schuller, R. E. Schaak, M. Terrones and J. A. Robinson, Recent Advances in Two-Dimensional Materials beyond Graphene, *ACS Nano*, 2015, 9(12), 11509–11539, DOI: [10.1021/acs.nano.5b05556](#).
- 7 C. Tan, X. Cao, X.-J. Wu, Q. He, J. Yang, X. Zhang, J. Chen, W. Zhao, S. Han, G.-H. Nam, M. Sindoro and H. Zhang, Recent Advances in Ultrathin Two-Dimensional Nanomaterials, *Chem. Rev.*, 2017, 117(9), 6225–6331, DOI: [10.1021/acs.chemrev.6b00558](#).
- 8 H. Zhang, Ultrathin Two-Dimensional Nanomaterials, *ACS Nano*, 2015, 9(10), 9451–9469, DOI: [10.1021/acs.nano.5b05040](#).
- 9 S. Mohsen Beladi-Mousavi and M. Pumera, 2D-Pnictogens: Alloy-Based Anode Battery Materials with Ultrahigh Cycling Stability, *Chem. Soc. Rev.*, 2018, 47(18), 6964–6989, DOI: [10.1039/C8CS00425K](#).
- 10 A. Mitrović, G. Abellán and A. Hirsch, Covalent and Non-Covalent Chemistry of 2D Black Phosphorus, *RSC Adv.*, 2021, 11(42), 26093–26101, DOI: [10.1039/D1RA04416H](#).
- 11 F. R. Fan, R. Wang, H. Zhang and W. Wu, Emerging Beyond-Graphene Elemental 2D Materials for Energy and
- 12 DOI: [10.1002/adma.201703771](#).
- 13 X. Yang, R. Wu, N. Xu, X. Li, N. Dong, G. Ling, Y. Liu and P. Zhang, Application and Prospect of Antimonene: A New Two-Dimensional Nanomaterial in Cancer Theranostics, *J. Inorg. Biochem.*, 2020, 212, 111232, DOI: [10.1016/j.jinorgbio.2020.111232](#).
- 14 X. Wang, J. Song and J. Qu, Antimonene: From Experimental Preparation to Practical Application, *Angew. Chem., Int. Ed.*, 2019, 58(6), 1574–1584, DOI: [10.1002/anie.201808302](#).
- 15 R. I. McCallum, Observations upon Antimony, *Proc. R. Soc. Med.*, 1977, 70(11), 756–763, DOI: [10.1177/003591577707001103](#).
- 16 J. Emsley, Nature's Building Blocks: An A–Z Guide to the Elements, *New ed., completely rev. and updated.*, Oxford University Press, Oxford, New York, 2011.
- 17 C. A. Tylenda; D. W. Sullivan and B. A. Fowler, Antimony, in *Handbook on the Toxicology of Metals*, Elsevier, 2015, pp. 565–579. , DOI: [10.1016/B978-0-444-59453-2.00027-5](#).
- 18 C. Liu, J. Shin, S. Son, Y. Choe, N. Farokhzad, Z. Tang, Y. Xiao, N. Kong, T. Xie, J. Seung Kim and W. Tao, Pnictogens in Medicinal Chemistry: Evolution from Erstwhile Drugs to Emerging Layered Photonic Nanomedicine, *Chem. Soc. Rev.*, 2021, 50(4), 2260–2279, DOI: [10.1039/D0CS01175D](#).
- 19 P. Bjerregaard; C. B. I. Andersen and O. Andersen, Ecotoxicology of Metals—Sources, Transport, and Effects on the Ecosystem, in *Handbook on the Toxicology of Metals*, Elsevier, 2015, pp. 425–459, DOI: [10.1016/B978-0-444-59453-2.00021-4](#).
- 20 S. Sundar and J. Chakravarty, Antimony Toxicity, *Int. J. Environ. Res. Public Health*, 2010, 7(12), 4267–4277, DOI: [10.3390/ijerph7124267](#).
- 21 *Chemistry of Arsenic, Antimony, and Bismuth*, ed. N. C. Norman, Blackie Academic & Professional, London, New York, 1st edn, 1998.
- 22 R. C. Fischer, Antimony: Inorganic Chemistry, in *Encyclopedia of Inorganic and Bioinorganic Chemistry*, ed. R. A. Scott, John Wiley & Sons, Ltd, Chichester, UK, 2016, pp. 1–13. , DOI: [10.1002/9781119951438.eibc0011.pub2](#).
- 23 C. E. C. Wood, T. M. Kerr, T. D. McLean, D. I. Westwood, J. D. Medland, S. Blight and R. Davies, State-of-the-art AlGaAs Alloys by Antimony Doping, *J. Appl. Phys.*, 1986, 60(4), 1300–1305, DOI: [10.1063/1.337300](#).
- 24 T. Li, Antimony and Antimony Alloys, in *Kirk-Othmer Encyclopedia of Chemical Technology*, John Wiley & Sons, Inc., Hoboken, NJ, USA, 2011, p. 011420091209.a01.pub3, DOI: [10.1002/0471238961.011420091209.a01.pub3](#).
- 25 K. Wang, K. Jiang, B. Chung, T. Ouchi, P. J. Burke, D. A. Boysen, D. J. Bradwell, H. Kim, U. Muecke and

- This journal is © The Royal Society of Chemistry 2023

- Chem. Soc. Rev., 2023, 52, 1288–1330 | 1323

- Hexagons, *Appl. Mater. Today*, 2022, **26**, 101360, DOI: [10.1016/j.apmt.2021.101360](#).
- 76 S. Zhang, Z. Yan, Y. Li, Z. Chen and H. Zeng, Atomically Thin Arsenene and Antimonene: Semimetal-Semiconductor and Indirect-Direct Band-Gap Transitions, *Angew. Chem., Int. Ed.*, 2015, **54**(10), 3112–3115, DOI: [10.1002/anie.201411246](#).
- 77 S. Cahangirov, M. Topsakal, E. Aktürk, H. Şahin and S. Ciraci, Two- and One-Dimensional Honeycomb Structures of Silicon and Germanium, *Phys. Rev. Lett.*, 2009, **102**(23), 236804, DOI: [10.1103/PhysRevLett.102.236804](#).
- 78 M. Zhao, X. Zhang and L. Li, Strain-Driven Band Inversion and Topological Aspects in Antimonene, *Sci. Rep.*, 2015, **5**(1), 16108, DOI: [10.1038/srep16108](#).
- 79 O. Ü. Aktürk, V. O. Özçelik and S. Ciraci, Single-Layer Crystalline Phases of Antimony: Antimonenes, *Phys. Rev. B: Condens. Matter Mater. Phys.*, 2015, **91**(23), 235446, DOI: [10.1103/PhysRevB.91.235446](#).
- 80 Y. Wang and Y. Ding, The Electronic Structures of Group-V–Group-IV Hetero-Bilayer Structures: A First-Principles Study, *Phys. Chem. Chem. Phys.*, 2015, **17**(41), 27769–27776, DOI: [10.1039/C5CP04815J](#).
- 81 M. Fortin-Deschênes, O. Waller, T. O. Menteş, A. Locatelli, S. Mukherjee, F. Genuzio, P. L. Levesque, A. Hébert, R. Martel and O. Moutanabbir, Synthesis of Antimonene on Germanium, *Nano Lett.*, 2017, **17**(8), 4970–4975, DOI: [10.1021/acs.nanolett.7b02111](#).
- 82 M. Fortin-Deschênes, H. Zschiesche, T. O. Menteş, A. Locatelli, R. M. Jacobberger, F. Genuzio, M. J. Lagos, D. Biswas, C. Jozwiak, J. A. Miwa, S. Ulstrup, A. Bostwick, E. Rotenberg, M. S. Arnold, G. A. Botton and O. Moutanabbir, Pnictogens Allotropy and Phase Transformation during van der Waals Growth, *Nano Lett.*, 2020, **20**(11), 8258–8266, DOI: [10.1021/acs.nanolett.0c03372](#).
- 83 T. Gupta, K. Elibol, S. Hummel, M. Stöger-Pollach, C. Mangler, G. Habler, J. C. Meyer, D. Eder and B. C. Bayer, Resolving Few-Layer Antimonene/Graphene Heterostructures, *npj 2D Mater. Appl.*, 2021, **5**(1), 1–11, DOI: [10.1038/s41699-021-00230-3](#).
- 84 P. Ares, F. Aguilar-Galindo, D. Rodríguez-San-Miguel, D. A. Aldave, S. Díaz-Tendero, M. Alcamí, F. Martín, J. Gómez-Herrero and F. Zamora, Mechanical Isolation of Highly Stable Antimonene under Ambient Conditions, *Adv. Mater.*, 2016, **28**(30), 6332–6336, DOI: [10.1002/adma.201602128](#).
- 85 K. S. Novoselov, Electric Field Effect in Atomically Thin Carbon Films, *Science*, 2004, **306**(5696), 666–669, DOI: [10.1126/science.1102896](#).
- 86 J. N. Israelachvili, *Intermolecular and Surface Forces: Revised*, 3d edn, Elsevier Science, Burlington, 2011.
- 87 B. Zhang, H. Zhang, J. Lin and X. Cheng, First-Principle Study of Seven Allotropes of Arsenene and Antimonene: Thermodynamic, Electronic and Optical Properties, *Phys. Chem. Chem. Phys.*, 2018, **20**(48), 30257–30266, DOI: [10.1039/C8CP05373A](#).
- 88 D. Singh, S. K. Gupta, Y. Sonvane and I. Lukačević, Antimonene: A Monolayer Material for Ultraviolet Optical Nanodevices, *J. Mater. Chem. C*, 2016, **4**(26), 6386–6390, DOI: [10.1039/C6TC01913G](#).
- 89 G. Liu, Z. Gao and J. Zhou, Strain Effects on the Mechanical Properties of Group-V Monolayers with Buckled Honeycomb Structures, *Phys. E*, 2019, **112**, 59–65, DOI: [10.1016/j.physe.2019.04.002](#).
- 90 D. R. Kripalani, A. A. Kistanov, Y. Cai, M. Xue and K. Zhou, Strain Engineering of Antimonene by a First-Principles Study: Mechanical and Electronic Properties, *Phys. Rev. B*, 2018, **98**(8), 085410, DOI: [10.1103/PhysRevB.98.085410](#).
- 91 P. Ares, J. J. Palacios, G. Abellán, J. Gómez-Herrero and F. Zamora, Recent Progress on Antimonene: A New Bidimensional Material, *Adv. Mater.*, 2018, **30**(2), 1703771, DOI: [10.1002/adma.201703771](#).
- 92 Y. Xu, B. Peng, H. Zhang, H. Shao, R. Zhang and H. Zhu, First-Principle Calculations of Optical Properties of Monolayer Arsenene and Antimonene Allotropes: First-Principle Calculations of Optical Properties of Monolayer Arsenene and Antimonene Allotropes, *Ann. Phys.*, 2017, **529**(4), 1600152, DOI: [10.1002/andp.201600152](#).
- 93 Z. Wu and J. Hao, Electrical Transport Properties in Group-V Elemental Ultrathin 2D Layers, *npj 2D Mater. Appl.*, 2020, **4**(1), 4, DOI: [10.1038/s41699-020-0139-x](#).
- 94 P. Ares, S. Pakdel, I. Palacio, W. S. Paz, M. Rassekh, D. Rodríguez-San Miguel, L. Aballe, M. Foerster, N. Ruiz del Árbol, J. Á. Martín-Gago, F. Zamora, J. Gómez-Herrero and J. J. Palacios, Few-Layer Antimonene Electrical Properties, *Appl. Mater. Today*, 2021, **24**, 101132, DOI: [10.1016/j.apmt.2021.101132](#).
- 95 S. Wang, W. Wang and G. Zhao, Thermal Transport Properties of Antimonene: An Ab Initio Study, *Phys. Chem. Chem. Phys.*, 2016, **18**(45), 31217–31222, DOI: [10.1039/C6CP06088A](#).
- 96 T. Zhang, Y.-Y. Qi, X.-R. Chen and L.-C. Cai, Predicted Low Thermal Conductivities in Antimony Films and the Role of Chemical Functionalization, *Phys. Chem. Chem. Phys.*, 2016, **18**(43), 30061–30067, DOI: [10.1039/C6CP05908B](#).
- 97 D.-C. Zhang, A.-X. Zhang, S.-D. Guo and Y. Duan, Thermoelectric Properties of β -As, Sb and Bi Monolayers, *RSC Adv.*, 2017, **7**(39), 24537–24546, DOI: [10.1039/C7RA03662K](#).
- 98 M. Fickert, M. Assebban, J. Canet-Ferrer and G. Abellán, Phonon Properties and Photo-Thermal Oxidation of Micro-mechanically Exfoliated Antimonene Nanosheets, *2D Mater.*, 2020, **7**, 025039, DOI: [10.1088/2053-1583/abb877](#).
- 99 X. Fan, Y. Li, L. Su, K. Ma, J. Li and H. Zhang, Theoretical Prediction of Tunable Electronic and Magnetic Properties of Monolayer Antimonene by Vacancy and Strain, *Appl. Surf. Sci.*, 2019, **488**, 98–106, DOI: [10.1016/j.apsusc.2019.05.133](#).
- 100 A. Bafekry, M. Ghergherehchi and S. Farjami Shayesteh, Tuning the Electronic and Magnetic Properties of Antimonene Nanosheets via Point Defects and External Fields: First-Principles Calculations, *Phys. Chem. Chem. Phys.*, 2019, **21**(20), 10552–10566, DOI: [10.1039/C9CP01378D](#).
- 101 C. He, M. Cheng and W. Zhang, Tunable Electronic and Magnetic Properties of Transition Metals Doped Antimonene: A First-Principles Study, *Mater. Res. Express*, 2018, **5**(6), 065059, DOI: [10.1088/2053-1591/aacdd7](#).

- Antimonene-Based X-Ray Radiosensitizer, *Adv. Funct. Mater.*, 2019, 1906010, DOI: [10.1002/adfm.201906010](#).
- 171 W. Han, P. Huang, L. Li, F. Wang, P. Luo, K. Liu, X. Zhou, H. Li, X. Zhang, Y. Cui and T. Zhai, Two-Dimensional Inorganic Molecular Crystals, *Nat. Commun.*, 2019, **10**(1), 4728, DOI: [10.1038/s41467-019-12569-9](#).
- 172 J. M. Englert, C. Dotzer, G. Yang, M. Schmid, C. Papp, J. M. Gottfried, H.-P. Steinrück, E. Spiecker, F. Hauke and A. Hirsch, Covalent Bulk Functionalization of Graphene, *Nat. Chem.*, 2011, **3**(4), 279–286, DOI: [10.1038/nchem.1010](#).
- 173 O. Üzengi Aktürk, E. Aktürk and S. Ciraci, Effects of Adatoms and Physisorbed Molecules on the Physical Properties of Antimonene, *Phys. Rev. B*, 2016, **93**(3), 035450, DOI: [10.1103/PhysRevB.93.035450](#).
- 174 V. Lloret, E. Nuin, M. Kohring, S. Wild, M. Löffler, C. Neiss, M. Krieger, F. Hauke, A. Görling, H. B. Weber, G. Abellán and A. Hirsch, Noncovalent Functionalization and Passivation of Black Phosphorus with Optimized Perylene Diimides for Hybrid Field Effect Transistors, *Adv. Mater. Interfaces*, 2020, **7**(23), 2001290, DOI: [10.1002/admi.202001290](#).
- 175 N. V. Kozhemyakina, J. M. Englert, G. Yang, E. Spiecker, C. D. Schmidt, F. Hauke and A. Hirsch, Non-Covalent Chemistry of Graphene: Electronic Communication with Dendronized Perylene Bisimides, *Adv. Mater.*, 2010, **22**(48), 5483–5487, DOI: [10.1002/adma.201003206](#).
- 176 T. Umeyama, T. Ohara, Y. Tsutsui, S. Nakano, S. Seki and H. Imahori, Noncovalent Functionalization of Few-Layered Antimonene with Fullerene Clusters and Photoinduced Charge Separation in the Composite, *Chem. – Eur. J.*, 2020, **26**(29), 6726–6735, DOI: [10.1002/chem.202001740](#).
- 177 T. García-Mendiola, C. Gutiérrez-Sánchez, C. Gibaja, I. Torres, C. Busó-Rogero, F. Pariente, J. Solera, Z. Razavifar, J. J. Palacios, F. Zamora and E. Lorenzo, Functionalization of a Few-Layer Antimonene with Oligonucleotides for DNA Sensing, *ACS Appl. Nano Mater.*, 2020, **3**(4), 3625–3633, DOI: [10.1021/acsanm.0c00335](#).
- 178 R. R. Nair, W. Ren, R. Jalil, I. Riaz, V. G. Kravets, L. Britnell, P. Blake, F. Schedin, A. S. Mayorov, S. Yuan, M. I. Katsnelson, H.-M. Cheng, W. Strupinski, L. G. Bulusheva, A. V. Okotrub, I. V. Grigorieva, A. N. Grigorenko, K. S. Novoselov and A. K. Geim, Fluorographene: A Two-Dimensional Counterpart of Teflon, *Small*, 2010, **6**(24), 2877–2884, DOI: [10.1002/smll.201001555](#).
- 179 F. Xing, J. Wang, Z. Wang, Y. Li, X. Gou, H. Zhang, S. Zhou, J. Zhao and Z. Xie, Covalently Silane-Functionalized Antimonene Nanosheets and Their Copolymerized Gel Glasses for Broadband Vis–NIR Optical Limiting, *ACS Appl. Mater. Interfaces*, 2020, **13**(1), 897–903, DOI: [10.1021/acsami.0c18738](#).
- 180 H. Yang, F. Li, C. Shan, D. Han, Q. Zhang, L. Niu and A. Ivaska, Covalent Functionalization of Chemically Converted Graphene Sheets via Silane and Its Reinforcement, *J. Mater. Chem.*, 2009, **19**(26), 4632–4638, DOI: [10.1039/b901421g](#).
- 181 J. A. Carrasco, A. Seijas-Da Silva, V. Oestreich, J. Romero, B. G. Márkus, F. Simon, B. J. C. Vieira, J. C. Waerenborgh, G. Abellán and E. Coronado, Fundamental Insights into the Covalent Silane Functionalization of NiFe Layered Double Hydroxides, *Chem. – Eur. J.*, 2020, **26**(29), 6504–6517, DOI: [10.1002/chem.201905397](#).
- 182 M. Barua, M. M. Ayyub, S. Acharya and C. N. R. Rao, Functionalization of Antimonene and Bismuthene with Lewis Acids, *Nanoscale*, 2022, **14**(37), 13834–13843, DOI: [10.1039/D2NR03206F](#).
- 183 M. M. Ayyub, M. Barua, S. Acharya and C. N. R. Rao, Covalent Functionalization of Antimonene and Bismuthene Nanosheets, *Small*, 2022, **18**(38), 2203554, DOI: [10.1002/smll.202203554](#).
- 184 J. Song, L. Xu, J. Li, J. Xue, Y. Dong, X. Li and H. Zeng, Monolayer and Few-Layer All-Inorganic Perovskites as a New Family of Two-Dimensional Semiconductors for Printable Optoelectronic Devices, *Adv. Mater.*, 2016, **28**(24), 4861–4869, DOI: [10.1002/adma.201600225](#).
- 185 X. Wang, J. He, B. Zhou, Y. Zhang, J. Wu, R. Hu, L. Liu, J. Song and J. Qu, Bandgap-Tunable Preparation of Smooth and Large Two-Dimensional Antimonene, *Angew. Chem., Int. Ed.*, 2018, **57**(28), 8668–8673, DOI: [10.1002/anie.201804886](#).
- 186 Z. Wang, R. Zhang, M. Zhao, Z. Wang, B. Wei, X. Zhang, S. Feng, H. Cao, P. Liu, Y. Hao, H. Wang, B. Xu, S. J. Pennycook and J. Guo, High-Yield Production of Stable Antimonene Quantum Sheets for Highly Efficient Organic Photovoltaics, *J. Mater. Chem. A*, 2018, **6**(46), 23773–23779, DOI: [10.1039/C8TA07214K](#).
- 187 Y. Song, Z. Liang, X. Jiang, Y. Chen, Z. Li, L. Lu, Y. Ge, K. Wang, J. Zheng, S. Lu, J. Ji and H. Zhang, Few-Layer Antimonene Decorated Microfiber: Ultra-Short Pulse Generation and All-Optical Thresholding with Enhanced Long Term Stability, *2D Mater.*, 2017, **4**(4), 045010, DOI: [10.1088/2053-1583/aa87c1](#).
- 188 Y. Song, Y. Chen, X. Jiang, W. Liang, K. Wang, Z. Liang, Y. Ge, F. Zhang, L. Wu, J. Zheng, J. Ji and H. Zhang, Nonlinear Few-Layer Antimonene-Based All-Optical Signal Processing: Ultrafast Optical Switching and High-Speed Wavelength Conversion, *Adv. Opt. Mater.*, 2018, **6**(13), 1701287, DOI: [10.1002/adom.201701287](#).
- 189 F. Zhang, J. He, Y. Xiang, K. Zheng, B. Xue, S. Ye, X. Peng, Y. Hao, J. Lian, P. Zeng, J. Qu and J. Song, Semimetal-Semiconductor Transitions for Monolayer Antimonene Nanosheets and Their Application in Perovskite Solar Cells, *Adv. Mater.*, 2018, **30**(38), 1803244, DOI: [10.1002/adma.201803244](#).
- 190 J. Chang, Novel Antimonene Tunneling Field-Effect Transistors Using an Abrupt Transition from Semiconductor to Metal in Monolayer and Multilayer Antimonene Heterostructures, *Nanoscale*, 2018, **10**(28), 13652–13660, DOI: [10.1039/C8NR03191F](#).
- 191 X. Sun, Z. Song, S. Liu, Y. Wang, Y. Li, W. Wang and J. Lu, Sub-5 Nm Monolayer Arsenene and Antimonene Transistors, *ACS Appl. Mater. Interfaces*, 2018, **10**(26), 22363–22371, DOI: [10.1021/acsami.8b03840](#).
- 192 J. Medina-Ramos, R. C. Pupillo, T. P. Keane, J. L. DiMeglio and J. Rosenthal, Efficient Conversion of CO₂ to CO Using

- Angew. Chem., Int. Ed.*, 2019, **58**(1), 134–138, DOI: [10.1002/anie.201808846](https://doi.org/10.1002/anie.201808846).
- 214 T. Xue, W. Liang, Y. Li, Y. Sun, Y. Xiang, Y. Zhang, Z. Dai, Y. Duo, L. Wu, K. Qi, B. N. Shivananju, L. Zhang, X. Cui, H. Zhang and Q. Bao, Ultrasensitive Detection of MiRNA with an Antimonene-Based Surface Plasmon Resonance Sensor, *Nat. Commun.*, 2019, **10**(1), 28, DOI: [10.1038/s41467-018-07947-8](https://doi.org/10.1038/s41467-018-07947-8).
- 215 M. K. Singh, S. Pal, A. Verma, R. Das and Y. K. Prajapati, A Nanolayered Structure for Sensitive Detection of Hemoglobin Concentration Using Surface Plasmon Resonance, *Appl. Phys. A: Mater. Sci. Process.*, 2021, **127**(11), 832, DOI: [10.1007/s00339-021-04985-w](https://doi.org/10.1007/s00339-021-04985-w).
- 216 B. Fatima, D. Hussain, S. Bashir, H. T. Hussain, R. Aslam, R. Nawaz, H. N. Rashid, N. Bashir, S. Majeed, M. N. Ashiq and M. Najam-ul-Haq, Catalase Immobilized Antimonene Quantum Dots Used as an Electrochemical Biosensor for Quantitative Determination of H₂O₂ from CA-125 Diagnosed Ovarian Cancer Samples, *Mater. Sci. Eng., C*, 2020, **117**, 111296, DOI: [10.1016/j.msec.2020.111296](https://doi.org/10.1016/j.msec.2020.111296).
- 217 Z. Q. Bu, Q. F. Yao, Q. Y. Liu, M. X. Quan, J. Y. Lu and W. T. Huang, Peptide-Based Sensing, Logic Computing, and Information Security on the Antimonene Platform, *ACS Appl. Mater. Interfaces*, 2022, **14**(6), 8311–8321, DOI: [10.1021/acsami.1c23814](https://doi.org/10.1021/acsami.1c23814).
- 218 Z. Chu, S. Zhang, B. Zhang, C. Zhang, C.-Y. Fang, I. Rehor, P. Cigler, H.-C. Chang, G. Lin, R. Liu and Q. Li, Unambiguous Observation of Shape Effects on Cellular Fate of Nanoparticles, *Sci. Rep.*, 2014, **4**(1), 4495, DOI: [10.1038/srep04495](https://doi.org/10.1038/srep04495).
- 219 B. Yameen, W. I. Choi, C. Vilos, A. Swami, J. Shi and O. C. Farokhzad, Insight into Nanoparticle Cellular Uptake and Intracellular Targeting, *J. Controlled Release*, 2014, **190**, 485–499, DOI: [10.1016/j.jconrel.2014.06.038](https://doi.org/10.1016/j.jconrel.2014.06.038).
- 220 G. Maiorano, S. Sabella, B. Sorce, V. Brunetti, M. A. Malvindi, R. Cingolani and P. P. Pompa, Effects of Cell Culture Media on the Dynamic Formation of Protein–Nanoparticle Complexes and Influence on the Cellular Response, *ACS Nano*, 2010, **4**(12), 7481–7491, DOI: [10.1021/nn101557e](https://doi.org/10.1021/nn101557e).
- 221 A. C. Sabuncu, J. Grubbs, S. Qian, T. M. Abdel-Fattah, M. W. Stacey and A. Beskok, Probing Nanoparticle Interactions in Cell Culture Media, *Colloids Surf., B*, 2012, **95**, 96–102, DOI: [10.1016/j.colsurfb.2012.02.022](https://doi.org/10.1016/j.colsurfb.2012.02.022).
- 222 F. Villanueva-Flores, A. Castro-Lugo, O. T. Ramírez and L. A. Palomares, Understanding Cellular Interactions with Nanomaterials: Towards a Rational Design of Medical Nanodevices, *Nanotechnology*, 2020, **31**(13), 132002, DOI: [10.1088/1361-6528/ab5bc8](https://doi.org/10.1088/1361-6528/ab5bc8).
- 223 A. Ivask, A. J. Mitchell, A. Malysheva, N. H. Voelcker and E. Lombi, Methodologies and Approaches for the Analysis of Cell–Nanoparticle Interactions, *Wiley Interdiscip. Rev.: Nanomed. Nanobiotechnol.*, 2018, **10**(3), e1486, DOI: [10.1002/wnan.1486](https://doi.org/10.1002/wnan.1486).

